Front. Struct. Civ. Eng. 2024, 18(11): 1730–1751
https://doi.org/10.1007/s11709-024-1125-8

RESEARCH ARTICLE

Electromechanical admittance-based automatic damage assessment in plate structures via one-dimensional CNN-based deep learning models

Thanh-Canh HUYNH[a,b], Nhat-Duc HOANG[a,b], Quang-Quang PHAM[c], Gia Toai TRUONG[d*], Thanh-Truong NGUYEN[e*]

[a] *Institute of Research and Development, Duy Tan University, Da Nang 550000, Vietnam*
[b] *Faculty of Civil Engineering, Duy Tan University, Da Nang 550000, Vietnam*
[c] *Bridge and Road Department, Danang Architecture University, Da Nang 550000, Vietnam*
[d] *Faculty of Civil Engineering and Technology, Dong A University, Da Nang 550000, Vietnam*
[e] *Industrial Maintenance Training Center, Ho Chi Minh City University of Technology (HCMUT), Ho Chi Minh City 700000, Vietnam*
[*] *Corresponding authors. E-mails: toaitg@donga.edu.vn; thtruong@hcmut.edu.vn*

© Higher Education Press 2024

ABSTRACT The conventional admittance approach utilizing statistical evaluation metrics offers limited information about the damage location, especially when damage introduces nonlinearities in admittance features. This study proposes a novel automated damage localization method for plate-like structures based on deep learning of raw admittance signals. A one-dimensional (1D) convolutional neural network (CNN)-based model is designed to automate processing of raw admittance response and prediction of damage probabilities across multiple locations in a monitored structure. Raw admittance data set is augmented with white noise to simulate realistic measurement conditions. Stratified K-fold cross-validation technique is employed for training and testing the network. The experimental validation of the proposed method shows that the proposed method can accurately identify the state and damage location in the plate with an average accuracy of 98%. Comparing with established 1D CNN models reveals superior performance of the proposed method, with significantly lower testing error. The proposed method exhibits the ability to directly handle raw electromechanical admittance responses and extract optimal features, overcoming limitations associated with traditional piezoelectric admittance approaches. By eliminating the need for signal preprocessing, this method holds promise for real-time damage monitoring of plate structures.

KEYWORDS convolutional neural network, electromechanical admittance, electromechanical impedance, piezoelectric transducer, damage localization, plate structure, deep learning, structural health monitoring

1 Introduction

The electromechanical admittance (EMA) technique, based on the electromechanical coupling characteristic of piezoelectric materials, has demonstrated its feasibility and practicality across diverse structural health monitoring (SHM) applications, including aerospace [1,2] and civil structures [3,4] and wind turbines [5,6]. Typically, the technique involves installing lightweight and fast-response piezoelectric transducer onto the surface of a target structure and tracking the changes in electromechanical impedance (EMI)/EMA responses as an indicator of structural integrity [7]. Since these responses contain rich information about the mechanical properties of the monitored structure, they exhibit sustainable alternations due to structural changes, damages, or defects. With a dependence on high-frequency structural excitations (usually exceeding 30 kHz), this method

Article history: Received Jan 12, 2024; Accepted Mar 19, 2024

exhibits heightened sensitivity to minor structural alterations within the near field of the piezoelectric transducers [8]. The technique is cost-effective and easy in implementation for complex structures [9], robust to early-stage damage [10], and offers multifaceted damage (including fatigue cracks [11], corrosion [12], loosened bolts [13], ice formation [14]) detection capabilities, low-cost wireless sensing [15–17].

Traditional methods for damage interpretation rely on quantifying EMA shifts using statistical metrics such as Root Mean Square Deviation (*RMSD*) and Cross-Correlation Deviation (*CCD*) [18–20]. Since the 2000s, Zagrai and Giurgiutiu [18] utilized the traditional EMI technique for crack detection in thin plates. Their study showed that the *CCD* metric, used in the high frequency band from 300 to 450 kHz, was found to be most successful for crack detection. Tinoco et al. [21] decoupled EMI measurements of piezoelectric transducer to identify and locate an induced damage in plate structures. In recent years, Tawie et al. [22] studied various piezoelectric transducer (PZT) attachment methods for EMI-based damage identification in composite plates. Their study compared the performance of several statistical damage metrics for quantifying the EMI change and damage identification. Le et al. [23] conducted a numerical study to examine the feasibility of the EMA technique for crack detection in a bearing plate. Their numerical study showed that the sensitivity of the EMI response to a crack was reduced with respect to the distance. In 2021, Zhu et al. [24] detected location of damage in a honeycomb sandwich composite plate with an array of PZT sensors. They developed a damage localization method by combining direct-coupled mechanical impedance with modified probability-weighted algorithm for enhancing the damage location imaging.

While the traditional metrics showed excellent results for damage alarming, the damage localization remains challenging. These metrics merely statistically measure changes in the EMA response, providing limited information about the damage state and location. Further, their sensitivity is contingent upon the trends in EMA signal variations. This, coupled with nonlinearities induced by structural damage in EMA features, poses challenges in identifying damage locations [13,25]. On the other hand, the reliability of diagnostic results is significantly influenced by the selection of effective frequency bands. In some instances, damage detection outcomes may be unreliable if improper frequency bands are utilized for EMA feature extraction [25,26]. These bands vary with the geometric, structural and mechanical properties of a host structure and are often determined through trial and error [10,27]. These hand-crafted preprocessing steps not only diminish the reliability of damage detection results but also hinder the automation of EMA-based damage detection.

To address shortcomings in traditional damage interpretation, scholars have investigated machine learning-based EMA methods. Lopes et al. [28] developed back-propagation artificial neural networks (ANNs) to predict damage from the EMI signals and successfully applied to identify damage in a scaled bridge section and a space truss structure. Min et al. [25] developed an ANN model that can automatically select frequency bands suitable for damage quantification. Other researchers developed a radial basis function network-based algorithm for temperature compensation [29]. In recent times, deep neural network algorithms have been applied in addressing various challenging problems in civil and structural engineering, including plate bending analysis [30–32], material design with topology optimization [33], the stochastic analysis of heterogeneous porous material [34], and heat transfer analysis of functionally graded materials. Among various algorithms, convolutional neural network (CNN) has shown excellent performance in damage detection in terms of accuracy and computational efficiency [35,36]. By combining feature extraction and damage classification within a unified architecture, the CNN offers an ability to autonomously extract and learn optimal damage-sensitive features from raw signals, while simultaneously reducing computational costs [35,37]. Nguyen et al. [38] developed a one-dimensional (1D) CNN-based regression model to predict prestress force in a post-tensioned structure from the raw EMI data set and later introduced various 1D CNN architectures for monitoring bolt-loosening [13]. Li et al. [39] integrated the EMI technique with a CNN-based regression model, quantitatively predicting and monitoring real-time concrete strength development. Two-dimensional (2D) CNN models were proposed for identifying damages in concrete structures [40,41]. Zhang et al. [42] introduced a 1D CNN-based admittance approach to automatically detect small-size damages in concrete structures. Recently, Ta et al. [43] developed a concrete stress prediction method based on a 1D CNN algorithm. de Oliveira et al. [44] developed a 2D CNN algorithm to diagnose the presence of damage in an aluminum specimen using pre-processed 2D images of raw EMI signals.

For admittance-based damage detection in plate structures, there are at least three remaining challenges. 1) Previous studies have predominantly concentrated on the development of CNN-based admittance algorithms to predict stress states or detect cracks in structural joints and concrete specimens, leaving damage localization in plate structures via deep learning of raw EMA data unexplored. 2) Existing EMA/EMI techniques for damage detection in plate structures often rely on manually extracting EMI features from predefined frequency bands using hand-crafted statistical metrics. This dependence can constrain the effectiveness of these

techniques in terms of accuracy and computational cost, and it impedes the potential for automated diagnosis. Moreover, when coupled with the nonlinearities induced by structural damage in EMA features, these factors pose challenges in identifying damage locations within a plate structure. 3) The CNN approach's damage prediction ability is still lack of investigation in terms of its generalization to handle variations in EMA data induced by noise.

This study proposes an alternative method for damage monitoring and localization in plate structures by integrating the admittance technique with a 1D CNN model. As compared with the previous studies, this study includes the following new contributions. 1) The proposed method can effectively localize damage in a plate structure using only a single transducer through 1D CNN-based deep learning of raw EMA responses. 2) By directly processing the raw data, the method can substantially decrease preprocessing costs associated with manual data transformation and damage-sensitive feature extraction. Consequently, it shows potential for real-time damage monitoring in plate structures. (3) Compared with previous 1D CNN-based methods, the proposed method shows superior performance in terms of accuracy with significantly lower testing error.

2 Piezoelectric admittance approach

The principle of the admittance technique involves monitoring the changes in EMI/EMA response, typically in the ultrasonic frequency range. The variations in EMI/EMA are sensitive to structural changes, damages, or defects, allowing for the early detection and identification of potential issues in a structural system. As shown in Fig. 1(a), a typical setup of the EMA measurement includes a PZT mounted on the surface of the plate, an EMA analyzer for exciting and recording the EMA response, and a computer for data visualization and result intepretation. Under the harmonic voltage excitation via the analyzer, the transducer is harmonically deformed based on the piezoelectric effect [10]. This deformation introduces a harmonic force $F(\omega)$ to the host plate. The plate's admittance describes its ability to respond to the applied force $F(\omega)$ and is defined as the ratio of the steady-state velocity to the force. The admittance response encapsulates the dynamic features of the interconnected transducer-plate system within a designated frequency range, holding a great potential for detecting structural changes in the host plate based on changes in the admittance response.

The coupling of the PZT-plate system can be described by a 1D simplified EMA model (Fig. 1(b)) [45]. The EMA response of this interconnected dynamic system can be deduced from the mechanical impedance of both the transducer and the plate. Assuming the host plate is defined by standard structural parameters: mass (m), damping (c), and stiffness (k). The mechanical impedance of the host structure ($Z_s(\omega)$) is calculated as the ratio of the induced force ($F(\omega)$) to the velocity of the host plate at the excitation point ($\dot{u}(\omega)$), as articulated in Eq. (1) [46]:

$$Z_s(\omega) = \frac{F(\omega)}{\dot{u}(\omega)} = c + m\frac{\omega^2 - \omega_n^2}{\omega} i, \tag{1}$$

where i represents the imaginary unit, ω_n is the natural

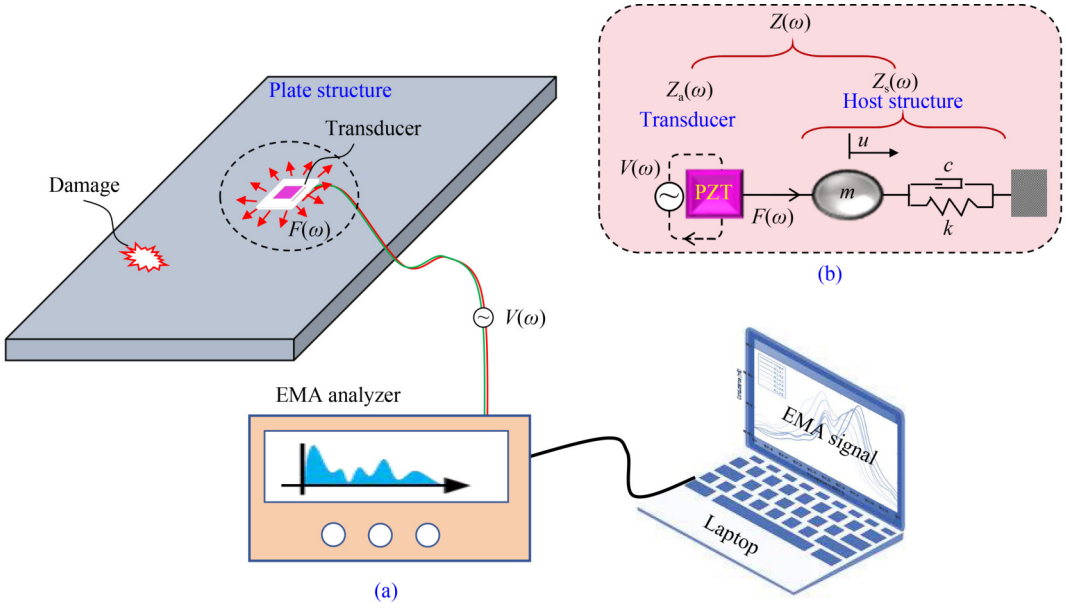

Fig. 1 The illustration of the admittance technique for damage identification in a plate structure: (a) the typical EMA measurement system; (b) the simplified EMA coupling model.

frequency of the host structure, and ω is the scanning frequency.

The EMI of the transducer-plate system $Z(\omega)$ can be simplified as a combined function involving both $Z_s(\omega)$ and $Z_a(\omega)$, as expressed in Eq. (2) and presented in the Ref. [47]. The EMA response $Y(\omega)$ is determined as the reciprocal of $Z(\omega)$, as outlined in Eq. (3).

$$Z(\omega)=\left\{i\omega\frac{w_a l_a}{t_a}\left[\hat{\varepsilon}_{11}^{T}-\frac{1}{Z_a(\omega)/Z_s(\omega)+1}d_{31}^2\hat{Y}_{11}^{E}\right]\right\}^{-1}, \quad (2)$$

$$Y(\omega)=\frac{1}{Z(\omega)}=\left\{i\omega\frac{w_a l_a}{t_a}\left[\hat{\varepsilon}_{11}^{T}-\frac{d_{31}^2\hat{Y}_{11}^{E}}{Z_a(\omega)\Big/\left[c+m\dfrac{\omega^2-\omega_n^2}{\omega}i\right]+1}\right]\right\}, \quad (3)$$

where $Z_a(\omega)$ represents the mechanical impedance of the transducer. The complex Young's modulus of the transducer (under no electric field) is signified by $\hat{Y}_{11}^{E}$; the complex dielectric constant (under no stress condition) is expressed by $\hat{\varepsilon}_{11}^{T}$; the 1D piezoelectric coupling constant (under no stress field) is denoted by d_{31}; the width, length, and thickness of the transducer are respectively represented by w_a, l_a, and t_a. It is noted that the transverse piezoelectric coupling constant, denoted as d_{31}, represents the coupling between an applied electric field in the longitudinal direction (direction 3−the poling direction) and the resulting strain in the transverse direction (direction 1−perpendicular to the direction 3). In contrast, the longitudinal piezoelectric coupling constant, denoted as d_{33}, signifies the coupling between an applied electric field in the longitudinal direction (direction 3) and the resulting strain in the same direction. Since the EMA technique proposed in this work utilizes the transverse mode, d_{33} was not considered in the mathematical equations of the 1D simplified model [47].

Equation (3) theoretically asserts that the resulting EMA response inherently encompasses the mechanical properties of the host structure (mass, damping, and stiffness). When damage occurs in the host plate, such as fatigue cracks or corrosion (indicating changes in stiffness or mass properties), the EMA response undergoes variations that reflect the altered mechanical properties. Therefore, monitoring these EMA changes aids in identifying structural damage. In practical applications, the EMA response is typically observed within a high-frequency range, frequently extending into ultrasonic bands. The short wavelength associated with high frequency enables the admittance technique to detect and monitor structural changes, representing early-stage structural damage.

3 Proposed damage identification method

3.1 Schematic of the method

Traditional feature extraction methods rely on manual intervention, which requires careful selection of EMA features and damage-sensitive frequency bands for effective damage identification [25,48]. Notably, an EMA feature considered effective for a particular host structure may not demonstrate the same effectiveness for others. Inappropriate use of the EMA feature can lead to suboptimal performance in detecting damage and estimating severity. Furthermore, the manual feature extraction process requires significant computational overhead, hindering automatic damage identification. Furthermore, since the traditional feature metrics such as only statistically quantify the changes in the EMA response [19,20], they could provide only limited information for damage detection. As reported in the previous studies [38,49], structural damage can induce nonlinearities in the EMA features. As a result, it is very difficult to determine the damage location in the plate based on only observing the trends of the traditional EMA features.

To address these challenges, a novel automated damage identification method for plate structures is proposed, integrating the admittance technique with a 1D CNN model, as illustrated in Fig. 2. The proposed approach directly processes raw EMA responses, autonomously extracting optimal EMA features, and predicting structural damage. By leveraging the 1D CNN's inherent capabilities for feature extraction, the method eliminates the need for manual feature extraction and data preprocessing steps [37,50]. The flowchart of the proposed method comprises the following steps. 1) Recording EMA signals from a target plate specimen subjected to structural damage at different location scenarios. 2) Augmenting the recorded EMA data by adding white noise to the raw EMA signals. This step broadens the data set, accounting for variations induced by diverse environmental conditions. 3) Partitioning the resultant EMA data into training and validation data sets using stratified-shuffle-split. This ensures a rigorous evaluation of the proposed method's performance and generalization across different scenarios. 4) Designing the architecture of the 1D CNN model for identifying structural damage and initializing the CNN model. 5) Training and testing the initiated 1D CNN model using K-fold cross-validation. 6) Detecting structural damage in the host plate, visualizing the results, and evaluating the accuracy of the proposed method.

3.2 One-dimensional convolutional neural network-based regression model

3.2.1 Network architecture

The regression model based on the 1D CNN algorithm is

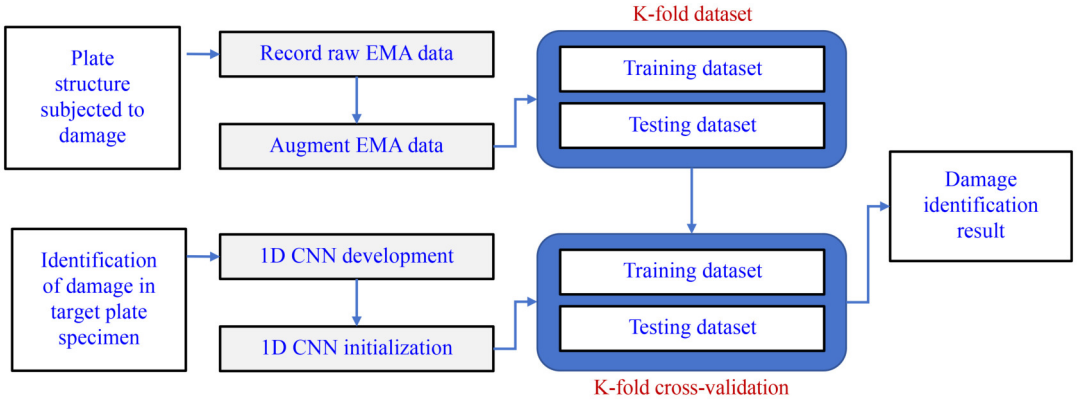

Fig. 2 The proposed CNN-based damage identification method for plate structures.

designed to automate the processing of raw EMA responses and facilitate automatic damage identification in plate structures. The network architecture, illustrated in Fig. 3, is formulated by drawing inspiration from the previous well-established models [38,51], ensuring effective learning and prediction of structural conditions. Comprising a total of 11 layers, each layer plays a distinct role in information processing. The input layer processes 1D raw EMA signals, and subsequent layers, including convolution, batch normalization, rectified linear unit (ReLU) activation, max-pooling, and fully-connected (FC) layers, contribute to implicit feature extraction. The output layer, a regression layer, predicts the damage index (*DI*) for each location on the target plate. The *DI* is then compared with a threshold to detect structural damage. It should be noted that the proposed network employs 1D convolutions to extract optimal impedance features from a 1D input signal. Although the outcome of damage localization in a plate is depicted in a 2D domain (Fig. 3), the network's output is, in fact, 1D. Each element of the output corresponds to the identification of the respective location on the plate.

3.2.2 Network's layer

The layer-specific information for the proposed CNN model is summarized in Table 1. The explanations of the layers are presented, as follows.

Input layer. The CNN model takes a 1D EMA signal as input with a size of $1 \times N$, where $N = 301$ denotes the number of frequency points in the EMA signal. To ensure a consistent distribution of inputs and facilitate error backpropagation, data normalization is implemented on each 1D EMA sample at the input layer. The *z*-score normalization method is utilized, as described in Eq. (4) [52]:

$$\mathrm{norm}Y(\omega) = \frac{Y(\omega) - \overline{Y}}{\sigma_Y}, \tag{4}$$

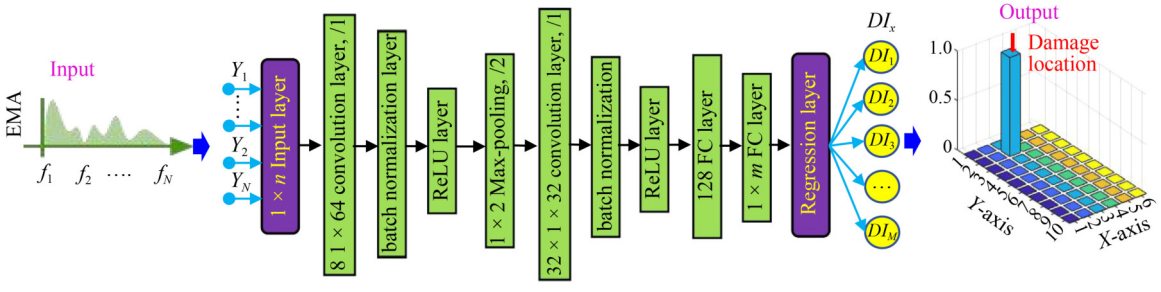

Fig. 3 The proposed CNN architecture for deep learning of raw EMA data and damage identification in a plate structure.

Table 1 The layer information of the proposed CNN model

Layer	Operator	Output shape	Kernel size [a]	Stride	Layer	Operator	Output shape	Kernel size	Stride
1	Input	1 × 301	–	–	6	Convolution	32 × 151	32 × 1 × 32	1
2	Convolution	8 × 301	8 × 1 × 64	1	7	Batch normalization	32 × 151	–	–
3	Batch normalization	8 × 301	–	–	8	ReLU	32 × 151	–	–
4	ReLU	8 × 301	–	–	9	FC	1 × 60	–	–
5	Max-pooling	8 × 151	1 × 2	2	10	Output	1 × 60	–	–

Note: a) Kernel size: Channel × Height × Width.

where norm$Y(\omega)$ and $Y(\omega)$ represent the normalized and original EMA signals, respectively; $\bar{Y}$ is the mean of the original signal and σ_Y is the corresponding standard deviation. Data normalization ensures a consistent distribution of input across each layer of the CNN, thereby altering the data distribution within each feature graph. This adjustment facilitates more straightforward error backpropagation and enhances network convergence. As demonstrated in Ref. [52], the z-score data normalization method exhibited exceptional performance during the training and testing phases of an EMA-based deep learning algorithm for damage detection. Consequently, this study has opted for the 'z-score' normalization method based on its proven effectiveness.

Convolutional layer. In the convolutional layer, kernels traverse the 1D input pattern during convolution with a specified stride (s) to extract features. Each 1D convolutional layer utilizes C channels of filters (kernels) with dimensions $1 \times Q$, where Q represents the temporal window covered by the filter. The mathematical formulation for a 1D convolutional layer is described as follows [53]:

$$y_r = f\left(\sum_{q=1}^{Q} w_q x_{r,q} + b\right), \tag{5}$$

where y_r represents the output of the unit r of the filter feature map of a size R; x is the 1D input portion overlapping with the filter; w denotes the connection weight of the convolutional filter; b is the bias term, $f(\cdot)$ is an activation function, q is the element's position in the temporal window. During the convolution process, the use of 'same' zero padding technique is applied to extend the input, ensuring the inclusion of information from the input's borders. This specific padding method preserves the exact size of both the input and output when the stride (s) is set to 1.

Batch normalization layer. In the training phase, the batch normalization layer plays a crucial role in normalizing and zero-centering the input based on the entire batch, representing the set of instances used for computing the loss and gradient during the training process [53]. This normalization approach enables the model to learn the optimal scaling of the input, thereby enhancing the efficiency of the training process. However, during the testing phase, the batch normalization layer operates differently. Instead of relying on batch-wide statistics, it utilizes precomputed mean and variance values obtained during the training phase. This strategy ensures consistent normalization and zero-centering procedures, aligning with the learned characteristics of the model.

ReLU layer. The role of the ReLU layer is to rectify negative values in the output of the preceding layer, mapping them to zero while preserving positive values. This layer serves a crucial function in minimizing computational costs and improving the overall efficiency of the training process. Mathematically, the ReLU operation for a given input value x is expressed as follows [54]:

$$\mathrm{ReLU}(x) = \max(0, x). \tag{6}$$

This operation introduces nonlinear characteristics into the model, empowering the network to discern complicated relationships within the data. The rectification of negative values fosters sparsity in activations, optimizing the learning process and bolstering the network's capacity to apprehend complex patterns in the data.

Max-pooling layer. The max-pooling layer employs a kernel on the preceding layer's output, with a designated stride (s), selecting the maximum value within the sliding window of the kernel. To safeguard crucial information at the input borders, zero-padding is applied. For an input sequence v of length K, the 1D max-pooling layer, characterized by a window size of $1 \times F$ and a stride s, systematically identifies the maximum value within each window, yielding an output sequence k. Mathematically, this process is expressed by [55]:

$$k_i = \max_{j=(i-1)s+1}^{is+F} v_j, \tag{7}$$

where the term k_i denotes the output at position i in the resultant sequence. The integration of this layer serves the dual purpose of efficiently diminishing the dimensionality of the input and facilitating error propagation during the back-propagation phase, thereby fostering the overall convergence of the network. The reduced size in representation space ensures invariance to minor translations of the input, empowering the network to identify distinct patterns at various locations within the feature map.

FC layer. A FC layer executes matrix multiplication between the input and a weight matrix, supplemented by the addition of a bias vector. In each FC layer, every unit establishes connections with all units in the preceding layer. The computation of each unit activation $y_j^{(l)}$ is obtained, as follows:

$$y_j^{(l)} = f\left(\sum_{i=1}^{I} w_{ji}^{(l)} x_i^{(l-1)} + b_j^{(l)}\right), \tag{8}$$

where I denotes the number of units in the previous layer, l represents the current layer, $w_{ji}^{(l)}$ is the weight of the connection between unit j of this layer and unit i in the previous layer, and $b_j^{(l)}$ is the bias term for the unit j. The activation function $f(\cdot)$ introduces nonlinearity, enabling the network to capture intricate relationships within the data. This FC layer plays a pivotal role in learning complex patterns and features by adjusting weights and biases throughout the training process.

Output regression layer. The network outputs a vector representing the *DI* of size $1 \times M$, where M is the number of damaged locations in the plate specimen (in this study, $M = 60$). Subsequently, the regression output layer utilizes the output obtained from the final FC layer to estimate the *DI* for each of the M locations. The regression layer calculates the half-mean-squared-error loss for regression tasks, as expressed by:

$$loss = \frac{1}{2}\sum_{k=1}^{R}(t_k - y_k)^2, \tag{9}$$

where R signifies the number of responses, t_k is the target output, and y_k denotes the prediction for the output k. During the training process of the networks, the lost function is minimized. To quantify the deviation of the prediction errors of a trained network, the three performance indicators including the root-mean-squared-error (*RMSE*), the mean-squared-error (*MSE*), and the mean-absolute-error (*MAE*) are calculated as follows:

$$\begin{aligned} RMSE &= \sqrt{\sum_{k=1}^{R}\frac{(t_k - y_k)^2}{R}}, \\ MSE &= \sum_{k=1}^{R}\frac{(t_k - y_k)^2}{R}, \\ MAE &= \sum_{k=1}^{R}\frac{|t_k - y_k|}{R}. \end{aligned} \tag{10}$$

3.2.3 Threshold-based damage identification

Outlier analysis is employed to identify potential damage in the plate. The *DI* for each location on the plate, representing the output of the 1D CNN, is compared with a predefined threshold for damage localization. First, the prediction error is computed, as follows:

$$e_k = t_k - y_k, \tag{11}$$

where e_k denotes the prediction error for the output k. Secondly, assuming the prediction error follows a normal distribution, the upper control limit (*UCL*) is computed as 3 standard deviations from the mean (99.73% confidence), as expressed by:

$$UCL = \mu_e + 3\sigma_e, \tag{12}$$

where μ_e is the mean of the prediction error e_k, and σ_e is the corresponding standard deviation. If the *DI* for a specific location on the plate is higher than the *UCL* threshold, that location is classified as 'damage'. Conversely, the location is classified as 'healthy' (undamaged).

3.3 Noise-injected data augmentation

The EMA signals can be influenced by various factors, such as material degradation and temperature changes [56–58]. Conducting comprehensive experiments that encompass all these factors can present substantial challenges in terms of both feasibility and cost. To pragmatically address the complexities associated with realistic measurement conditions, data augmentation emerges as a viable solution [38,59]. In this study, we selected a data augmentation method based on injection of Gaussian noise into the recorded EMA signals. This method is widely accepted for simulating noise effects on the EMA technique [60,61]. By employing two adjustable parameters, namely mean zero and standard deviation, the method provides flexibility to enable the injection of noise at different levels. The formulation for injecting noise into the EMA signal is expressed by:

$$Y_{noisy}(\omega) = Y(\omega) + \epsilon(\omega), \tag{13}$$

where $Y(\omega)$ is the measured EMA signal, $Y_{noisy}(\omega)$ is the corresponding noise-contaminated signal, and $\epsilon(\omega)$ represents the noise vector.

3.4 K-fold cross validation and accuracy evaluation

To mitigate the instability in model performance evaluation resulting from a single data split and to counteract overfitting challenges during the training phase, our study employs a specialized K-fold cross-validation technique known as stratified-shuffle-split [62]. By repeatedly training and testing the network on different subsets of the data, K-fold cross-validation allows the network to learn from various parts of the data set, contributing to better generalization. In particular, the K-fold cross-validation process divides the measured raw EMA signals into five distinct folds ($K = 5$). Each fold undergoes random division, allocating 80% of the data to the training set and 20% to the evaluation set. Subsequently, individual fold performance is evaluated, and the average performance is aggregated to characterize the overall proficiency of the K-folds.

The K-fold cross-validation process for evaluating the 1D CNN model comprises two key stages. 1) Data configuration, and 2) model training and evaluation. In the first stage, raw EMA signals and their corresponding structural conditions of the target plate are categorized into training and evaluation folds. In the subsequent stage, the 1D CNN regression model is initialized. Training fold data sets, consisting of EMA data sets and associated structural conditions, are utilized to train the 1D CNN model, while evaluation fold data sets assess the model's performance on previously unseen data.

The accuracy of the deep learning model is evaluated as

follows. (1) The probabilities of damage occurrence for all potential damage locations on the plate (i.e., the final output of the model) are compared with the *UCL* threshold for damage classification. If the probability of a location is over the *UCL* threshold, that location is classified as 'damage'. Otherwise, it is classified as 'healthy'. (2) For each test, the damage classification result is compared with the ground-truth and the accuracy is computed as the ratio of the number of correctly-classified locations to the number of all potential damage locations. (3) The accuracy of each fold is computed by averaging the accuracy of all tests in that fold.

4 Experimental investigation

4.1 Test-setup

The splice plate of a bolted connection was chosen for experimental evaluation of the proposed method. As depicted in Fig. 4(a), the test structure is a rectangular plate with dimensions 200 mm × 380 mm and a thickness of 10 mm. Four small foam blocks, each measuring 20 mm × 20 mm × 10 mm, provide support to the testing plate. To enhance the EMA response from the plate, the 'PZT interface technique', developed in a prior study [56], was employed as the piezoelectric transducer device. As shown in Fig. 4(b), the transducer device was situated at the center of the bottom of the connection plate via bonding layers. The device consists of a PZT-5A patch (20 mm × 20 mm × 0.51 mm) affixed to an aluminum base (100 mm × 33 mm × 5 mm). The aluminum base is structured with two outer connected parts, each with a thickness of 5 mm, and a middle unconnected part with a thickness of 4 mm.

Harmonic excitation of 1V amplitude was applied to the transducer, and the resulting EMA signal was measured within a frequency range of 10–25 kHz (301 points and 50 Hz interval) using a HIOKI 3532 impedance analyzer, as depicted in Fig. 4(c). The chosen scanning frequency range was tailored to capture robust resonant responses, critical for effective damage identification, in alignment with previous recommendations [63,64]. Laboratory temperature was maintained at 22 °C through air conditioning to ensure data consistency and minimize the potential influence of temperature variation on the EMA signal.

4.2 Measured admittance response

The EMA response was obtained under simulated structural damage at various locations on the plate. The damage simulation technique, utilizing added mass, was employed to represent stiffness/mass alterations in the plate. This technique mimics the effects of cracks or corrosion without causing harm to the test structure [48,65,66]. The mass was magnetically attached to the top surface of the splice plate (Fig. 4(a)). The mass is a cylinder-shaped block with a height of 0.02 m, a diameter of 0.04 m, a weight of 0.174 kg. The mass was respectively added at 60 intersections of a 2-cm grid marked over a quarter of the splice plate (Fig. 4(d)). Totally, 61 testing cases including Intact + 60 Damage cases (D_{XY} where X = 1:6 and Y = 1:10) were conducted during the experiment.

For each of the testing cases, the EMA response was

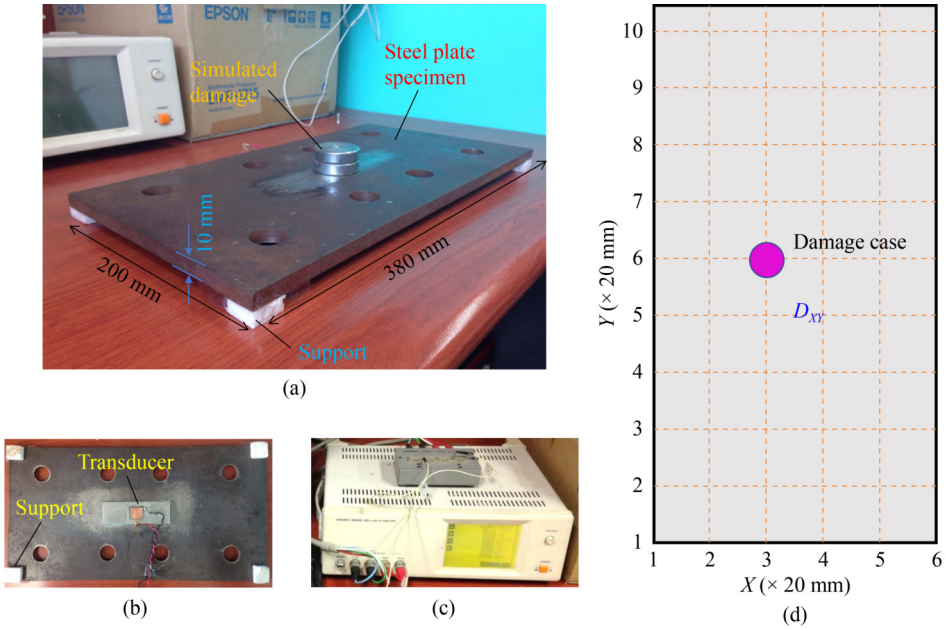

Fig. 4 The experimental setup: (a) the test plate specimen with added mass as a simulated damage; (b) the EMA analyzer; (c) the EMA transducer at the bottom surface; (d) the grid of damage locations over a quarter of the test plate specimen.

measured and repeated four times. Totally, 244 EMA signals corresponding to 61 testing cases were obtained. Figure 5(a) shows the sample EMA signal of the intact state. The implementation of the PZT interface technique generated strong resonances within 10–25 kHz. The most significant EMA responses occur in the frequency range of 15–18 kHz. Strong resonances should contain significant information about the structural properties of the host plate and therefore they should be employed for damage identification [63]. Figure 5(b) shows the EMA signals corresponding to different damage locations in the test specimen. It is observed that the resonant EMA responses sensitively vary with the location of added mass. The most damage-sensitive band is 15–18 kHz (Fig. 5(c)). In this range, the shift of resonant frequencies is approximately within the range of 0.3–0.5 kHz.

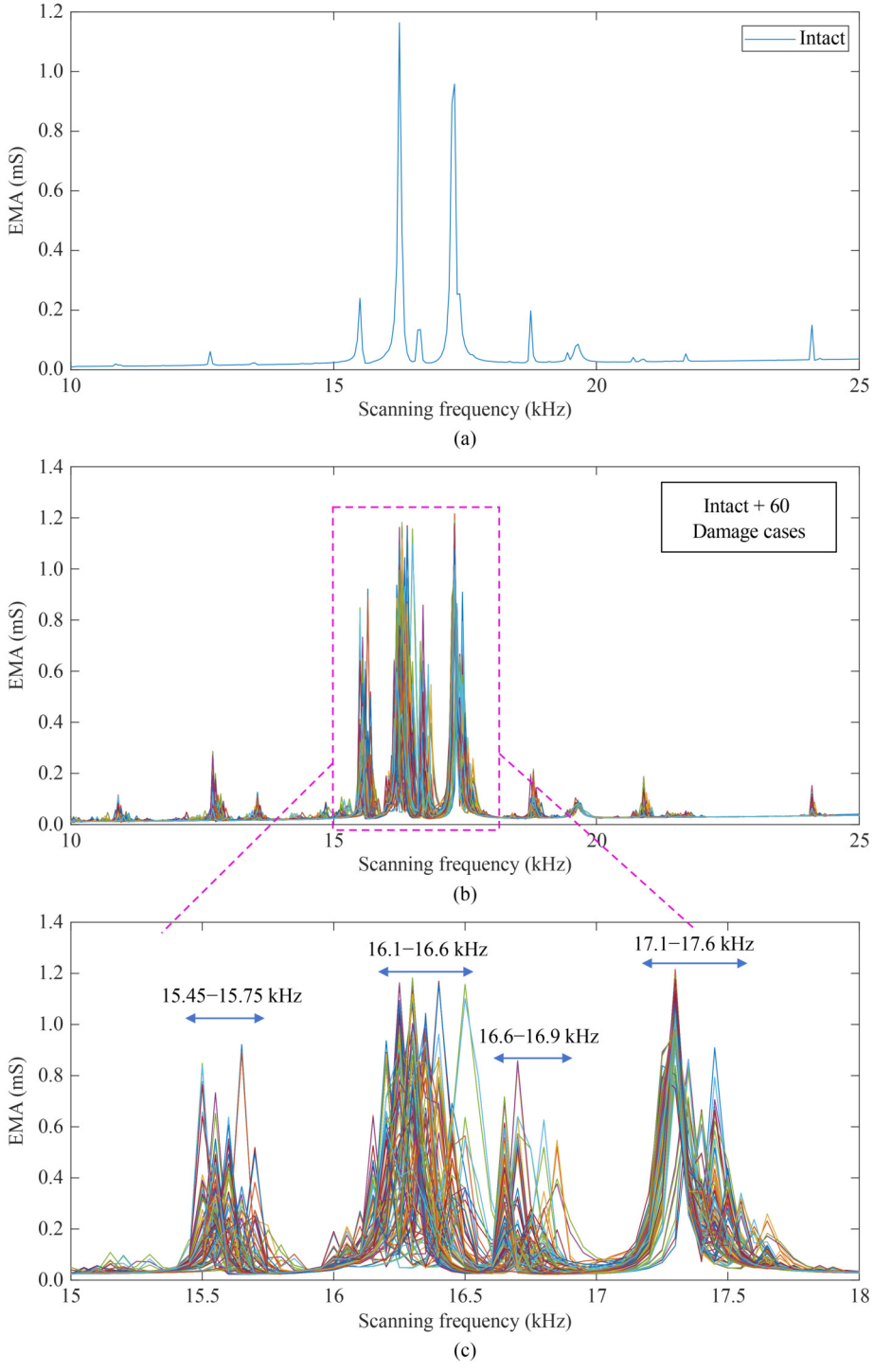

Fig. 5 The measured EMA signals: (a) the intact case; (b) the Intact + 60 Damage cases; (c) the significant resonance band in 15–18 kHz.

4.3 Damage monitoring using traditional metrics

To offer an assessment of overall structural integrity of the plate specimen, the EMA features were extracted using the traditional approaches. Widely accepted damage metrics for the admittance technique, such as *RMSD* and *CCD* were calculated [19,20]. Typically, these damage indices approach zero when the plate structure is in a healthy state and increase beyond zero with the onset of damage. The *RMSD* damage index is defined by Eq. (14) [20]:

$$RMSD = \sqrt{\sum_{i=1}^{N}[Y^*(\omega_i) - Y(\omega_i)]^2 \Big/ \sum_{i=1}^{N}[Y(\omega_i)]^2}, \quad (14)$$

where $Y(\omega_i)$ is the EMA signal at the healthy state (i.e., Intact case) for the ith frequency and $Y^*(\omega_i)$ is the EMA signal at the damage state; and N is the quantity of scanning frequencies (N = 301 in this study). The *CCD* damage index is defined by Eq. (15) [19]:

$$CCD = 1 - \frac{1}{N-1}\frac{\sum_{i=1}^{N}\left(Y(\omega_i) - \overline{Y}\right)\left(Y^*(\omega_i) - \overline{Y^*}\right)}{\sigma_Y \sigma_{Y^*}}, \quad (15)$$

where $\overline{Y}$ and $\overline{Y^*}$ are the means of the EMA signals at the healthy state and the damage state, respectively; σ_Y and σ_{Y^*} are the corresponding standard deviations of the EMA signals.

Figures 6(a) and 6(b) show the contours of the *RMSD* and *CCD* metrics computed over the 60 damage locations on the splice plate, respectively. The EMA of the intact case was used as the baseline. The metrics were averaged over four replicate EMA measurements. Generally, the magnitude of the *CCD* metric is lower than the *RMSD* metric but they exhibit similar damage-sensitivity patterns. It is observed that the sensitivity of the EMA response to structural damage is dependent on the damage location. Notably, the damage cases D_{14}, D_{24}, D_{34}, D_{23}, D_{66}, and D_{67} exhibit low sensitivity to damage compared to others. In contrast, the EMA response of the cases D_{21},

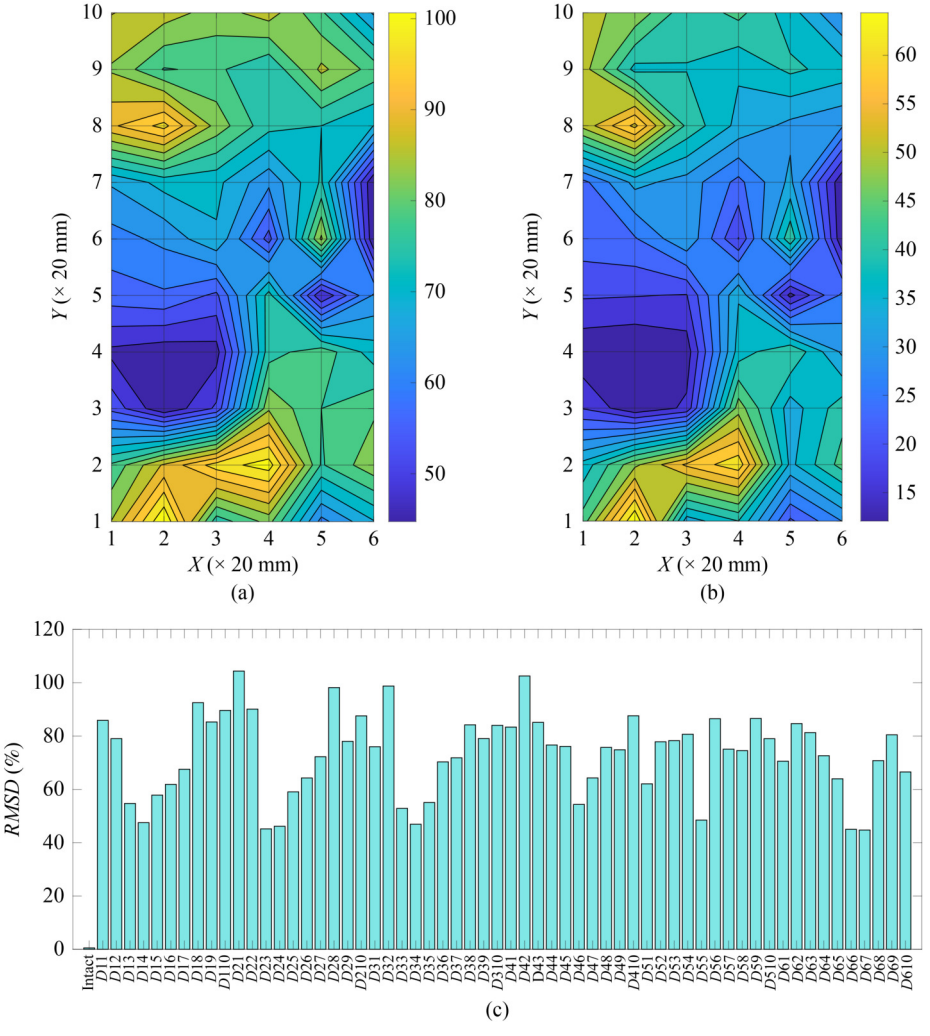

Fig. 6 The quantitative damage evaluation using traditional approaches: (a) *RMSD* contour; (b) *CCD* contour; (c) *RMSD* metric vs damage locations.

D_{28}, D_{32}, and D_{42} are the most sensitive to damage. Despite variations in damage sensitivity, the magnitudes of the damage metrics are consistently higher than zero for all damage cases, signifying damage to the plate specimen.

The analysis of the correlation chart between *RMSD* and the damage location in Fig. 6(c) indicates that numerous damage locations result in comparable magnitudes of the damage metric. Additionally, the nonlinear nature of *RMSD* with the damaged distance is observed. Specifically, as the distance along the *Y*-axis increases from 0 to 8 cm (D_{11}–D_{14}), the *RMSD* magnitude gradually decreases. After reaching a minimum at the position of 8 cm (D_{14}), this metric subsequently increases, peaking at the damaged location of 16 cm (D_{18}). Following a slight decrease at the position of 18 cm (D_{19}), it rises again at the location of 20 cm (D_{110}). Consequently, relying solely on the magnitudes of these two metrics poses challenges in precisely determining the location of damage on the plate. These metrics only provide information about the presence or absence of damage on the plate. Therefore, it is necessary to develop an alternative method to accurately determine the location of damage on the plate.

5 Performance evaluation of the proposed method

5.1 Data configuration

For each of the 61 testing cases, four EMA samples were measured repeatedly. In each sample, 301 data points were collected from the frequency range of 10–25 kHz with a 50 Hz interval. Consequently, an EMA databank of 73444 data points was obtained, corresponding to 61 different structural conditions of the plate (i.e., Intact + D_{XY} where X = 1:6, Y = 1:10). In real-world applications, EMA signatures are influenced by external disturbances such as noise conditions. To account for realistic scenarios and for data augmentation purposes, each EMA signal was injected with random white Gaussian noise, with a standard deviation ranging from 0% to 5% (0.5% intervals) of the signal amplitude. Figure 7(a) illustrates sample noise signals added to the EMA data. In the zoomed-in view in Fig. 7(b), the added noises in the 15–18 kHz band exhibit the most significant magnitudes, corresponding to the strong resonances. The amplitude changes in the EMA signal become more noticeable with higher noise percentages.

The resultant EMA databank consists of the input of 2684 EMA signals (807884 data points) and the output representing the 61 structural conditions of the plate specimen. The target output consists of the *DI* data where DI_{XY} is assigned to 1 if the location (X,Y) is damaged and 0 if the location (X,Y) is healthy. The stratified shuffle-split technique [62] was employed to randomly partition the acquired databank (2684 EMA signals) into 5-fold data sets denoted as Fold 1 through Fold 5. Each of the 5-folds is composed of an evaluation set (20%) and a training data set (80%). Figure 8 depicts the distribution of testing EMA samples within the evaluation set for each fold. The application of the stratified shuffle-split technique ensures that each fold maintains a representative distribution of the target structural conditions, thereby enhancing the distinctiveness of each split data set for training and evaluating the proposed 1D CNN model.

All training and testing experiments are conducted on a desktop computer equipped with an Intel Core i7-8700 CPU running at 3.2 GHz, 32 GB DDR4 memory, and a GeForce GT 1030 GPU. The implementation of the 1D CNN is carried out in the Matlab program.

5.2 Damage localization using the proposed method

To minimize the loss function and iteratively update the parameters of the network, the stochastic gradient descent with momentum optimization algorithm was utilized. The

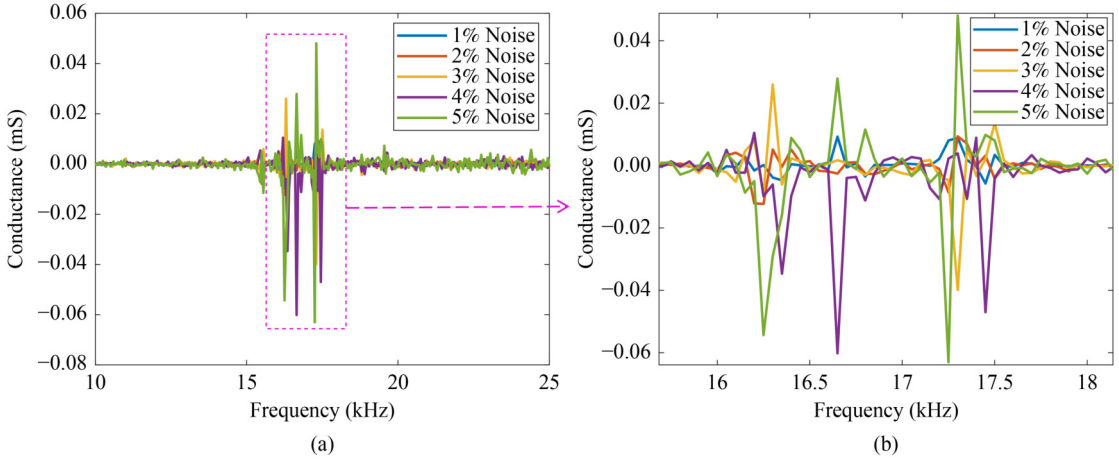

Fig. 7 The added noises to the EMA signals for data augmentation: (a) 10–25 kHz; (b) 15.75–18.25 kHz.

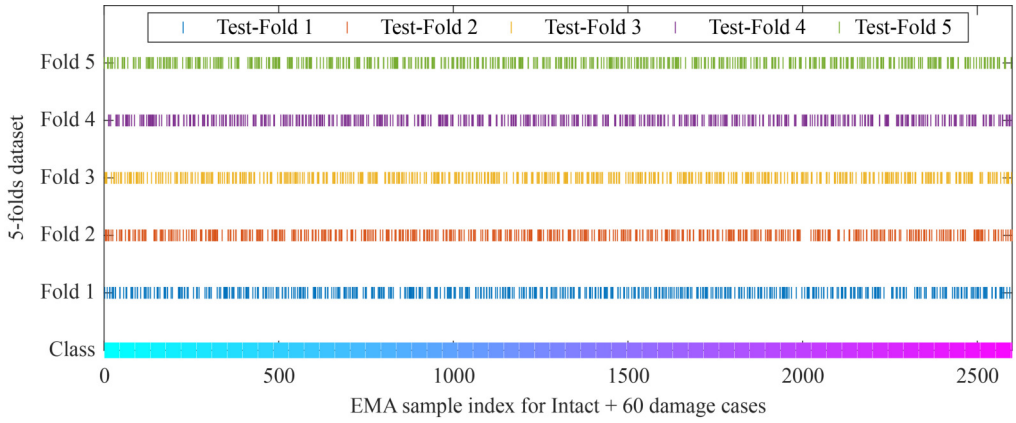

Fig. 8 The distribution of the testing samples in each fold for K-fold cross validation.

hyper-parameters were configured with a mini-batch size of 8, momentum of 0.9, learning rate of 0.001, learning rate drop factor of 0.1, and a learning rate drop period of 20. The training process spans 20 epochs. Shuffling of the training data at the commencement of each training epoch was implemented to enhance learning and improve the generalization capability of the machine learning model. This practice aids in mitigating overfitting and contributes to the robustness of the trained model.

Figure 9 illustrates the training outcomes of the proposed 1D CNN regression model for damage identification in plate structures. As depicted in Fig. 9(a), the training loss for the 5-folds significantly decreases after the initial 40 iterations. In parallel, the training error (i.e., *RMSE*) corresponding to the 5-folds also exhibits a substantial reduction after the initial iterations, as shown in Fig. 9(b). Subsequently, the training *RMSE* continues to decrease but at a slower rate, stabilizing after over 5300 iterations, indicating the convergence of the 1D CNN model.

The evaluation results for each of the 5-folds are visually depicted in Figs. 10(a)–10(e), and a sample ground-truth illustration (i.e., of Fold 5) is showcased in Fig. 10(f). In these 3D plots, the horizontal axis corresponds to the 60 potential damage locations within the plate, the lateral axis signifies the testing samples, and the vertical axis illustrates the *DI* values. It is apparent from the observation that the *DI* values predicted by the proposed CNN model for the 60 locations closely coincide with each other and exhibit a strong agreement with the ground-truth sample.

The distribution of prediction errors for the 5 folds is depicted in Figs. 11(a)–11(e), illustrating that the errors adhere to normal distributions. Subsequently, the *UCL* across the 5 folds was established for damage classification, as shown in Fig. 11(f). The *UCL* value exhibits slight variations across folds, ranging from 0.0361 to 0.0460. The *UCL* planes are also plotted in Figs. 10(a)–10(e). The *DI* values for undamaged locations consistently fall below the *UCL* plane for all folds, whereas those for damaged locations exceed the threshold and reach approximately 1. Some positions on the plate specimen, although undamaged, exhibit *DI* values slightly surpassing the *UCL* threshold. Nevertheless, the extent of these exceedances is negligible. Several typical diagnostic results are depicted in Fig. 12. As observed in the figure, the simulated damage locations in the plate specimen were successfully detected. The *DI* values of the damaged locations stand out compared to the remaining positions.

Figure 13(a) illustrates the testing *RMSE* across 5 folds, ranging from 0.0177 to 0.0219, with a mean of 0.0192, equivalent to approximately 2% of the *DI* of damaged locations. The low testing *RMSE* values indicate the high accuracy of the proposed 1D CNN model for damage identification in plate structures. The testing *MSE* across 5 folds, depicted in Fig. 13(b), ranges from 0.00031 to 0.00048, with a mean of 0.00037. Similarly, the testing *MAE* across 5 folds, illustrated in Fig. 13(c), ranges from 0.0133 to 0.0164, with a mean of 0.0144. These indicators consistently demonstrate low values, affirming the good performance of the deep learning model. The testing accuracy of the model across 5 folds, assessed by comparing with the *UCL* threshold, is plotted in Fig. 13(d). The accuracy of the proposed model is remarkably high, ranging from 97.15% to 98.35%, with an average value of 97.97%.

The attained results underscore the effectiveness of the proposed 1D CNN regression model. The model exhibits the capability to directly handle raw EMA data sets and acquire optimal EMA features, thereby overcoming the limitations of traditional damage metric approaches in the presence of nonlinearity within damage characteristics, as elucidated in Subsection 4.3. Additionally, the proposed method can autonomously identify damage locations without the need for signal preprocessing steps, reducing computation time and costs, demonstrating its potential

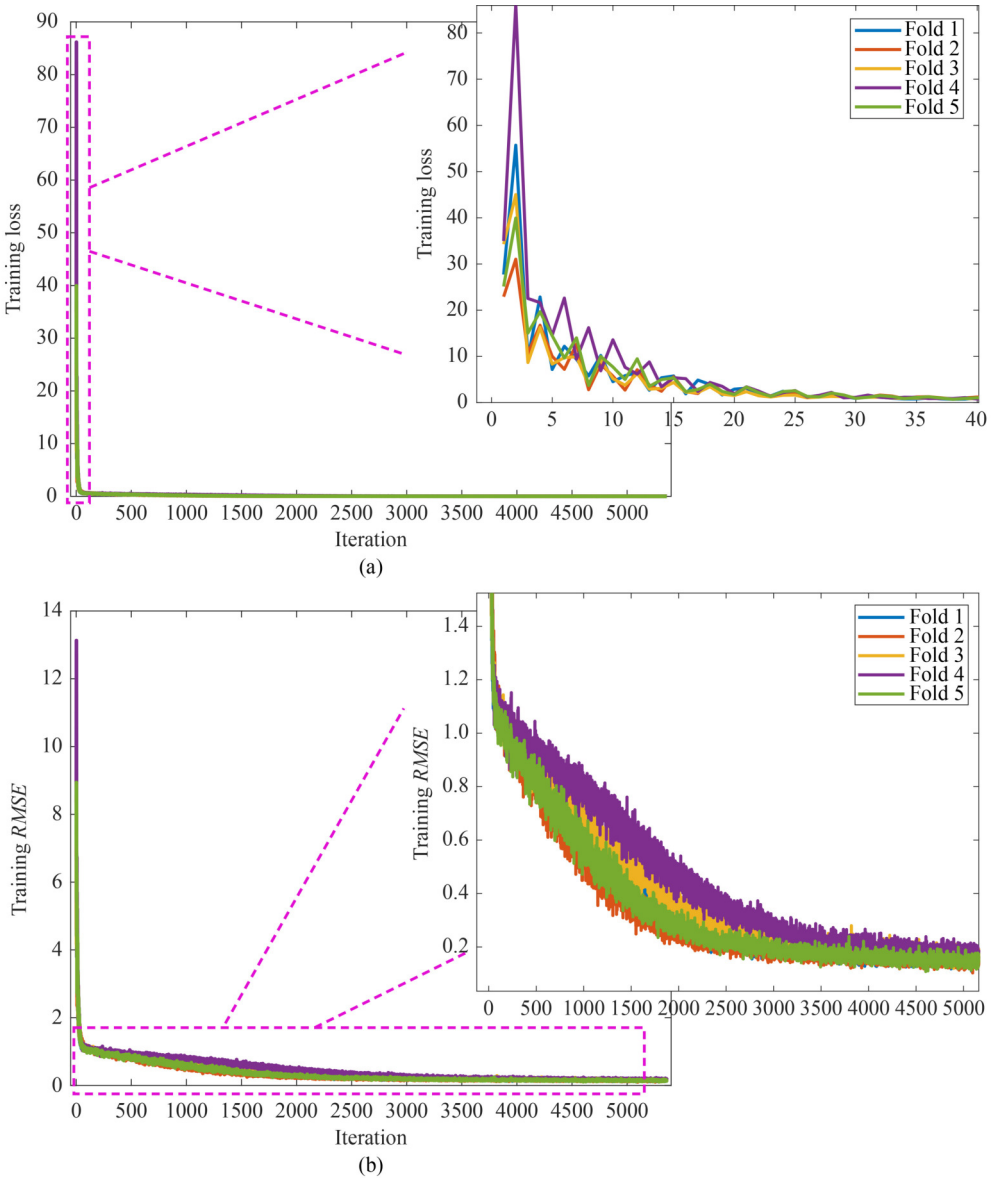

Fig. 9 The training of the proposed 1D CNN: (a) training loss; (b) training *RMSE*.

for real-time damage monitoring and assessment applications.

5.3 Comparison of deep learning models

In this section, we assess the performance of the proposed model by comparing it with two established 1D CNN models introduced by Nguyen et al. [38] and Ai et al. [67], respectively. Both benchmark models undergo training and validation using the identical data sets of the 5-folds through the K-fold cross-validation method. The training algorithm and parameters are set according to the specifications in Subsection 5.1, with the number of epochs determined based on the convergence of the training loss.

Figure 14 illustrates the performance comparison between the current study and previous research using the *RMSE*, *MSE*, and *MAE* indicators. The results indicate the superior performance of the proposed method. All three performance indicators of the proposed method exhibit the lowest values. Nguyen's and Ai's models exhibit testing *RMSE* values approximately 5 and 6 times higher than the proposed model, respectively. Similarly, their testing *MSE* values are approximately 27 and 37 times higher than the proposed model, while their *MSE* values are approximately 3.2 and 2.6 times higher than the *MAE* of the proposed model. The specific outcomes of damage identification in the plate specimen using these two established models are elaborated in the subsequent sections.

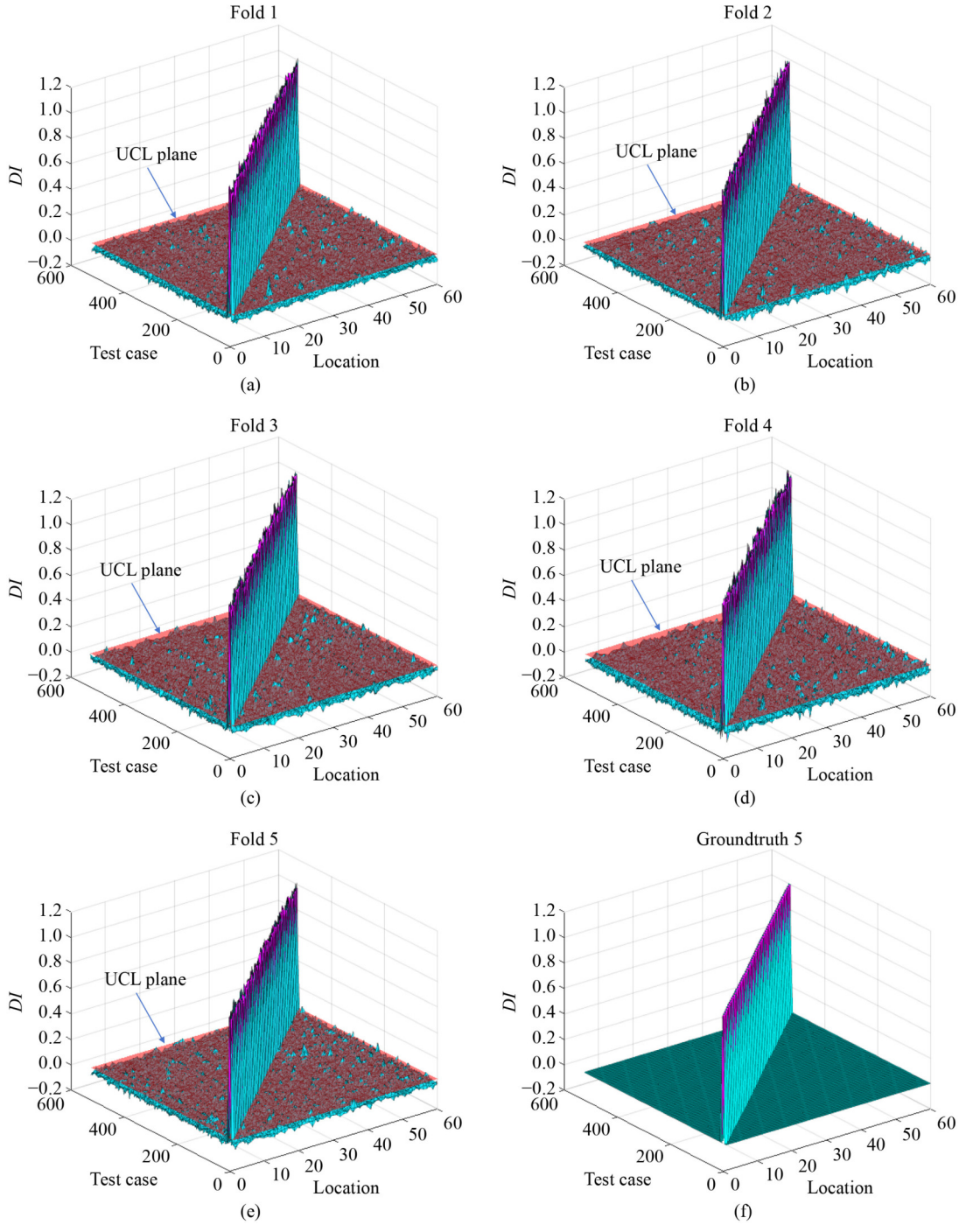

Fig. 10 The testing results across 5 folds: (a) Fold 1; (b) Fold 2; (c) Fold 3; (d) Fold 4; (e) Fold 5; (f) sample ground-truth (Fold 5).

5.3.1 Ai's model

The input and output layers of the 1D CNN model proposed by Ai et al. [67] were adapted to accommodate the EMA data set in this study. Particularly, the input layer of the model was adjusted to learn from the EMA data of size 1×301 ($N = 301$), while the output layer of the model was replaced with a regression output layer with an output size of 1×60 ($M = 60$).

The training loss and evaluation results across 5 folds for Ai's method are presented in Fig. 15. Across all folds, a substantial reduction in loss is observed in the initial 6000 training iterations, as shown in Fig. 15(a). Subsequently, the loss exhibits a gradual decrease over the next 5000 iterations and remains stable in the remaining iterations. As depicted in Fig. 15(b), during the final iterations, the loss mostly varies between 0.30 and 0.35. A good prediction model should have low testing

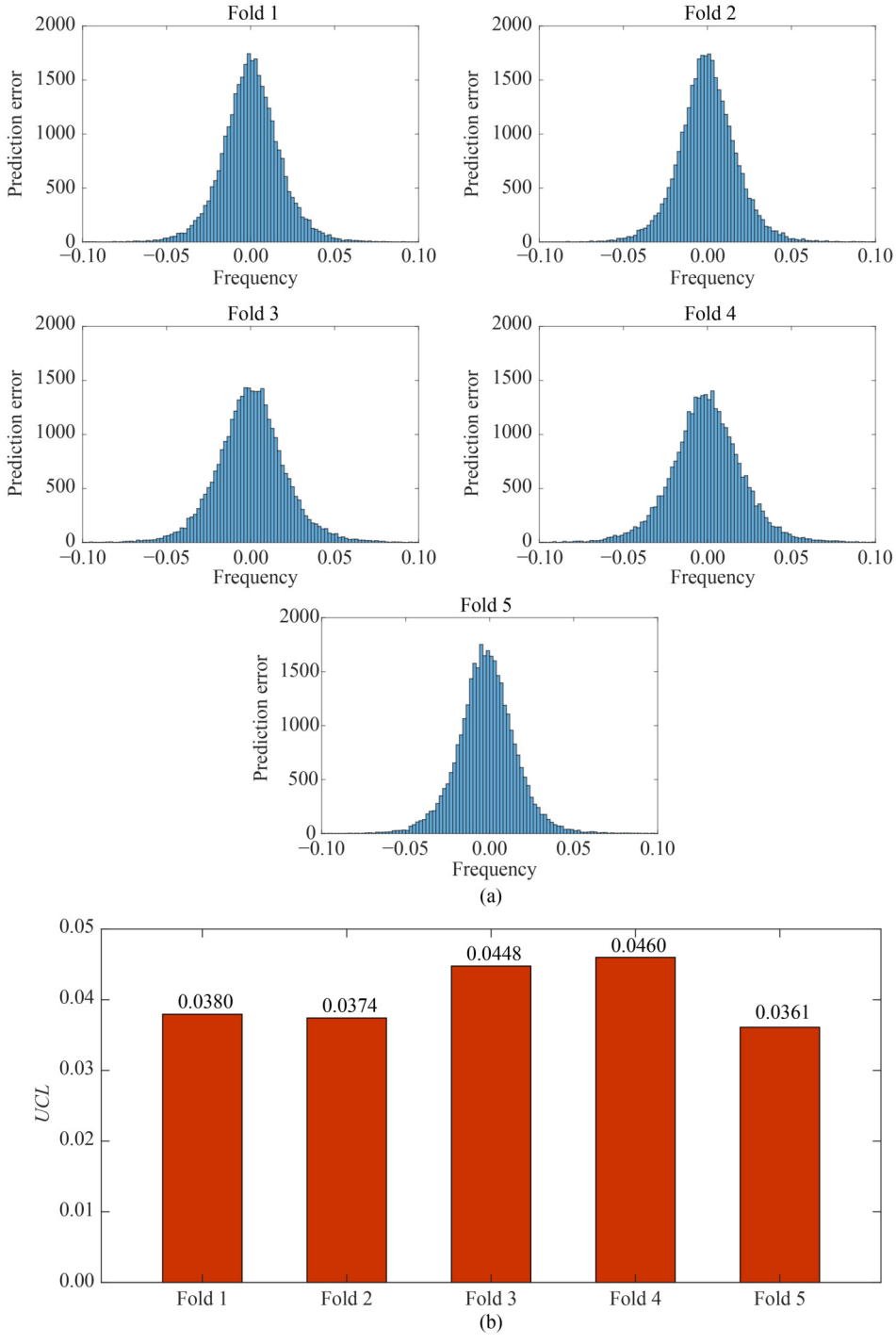

Fig. 11 The *UCL* thresholds for damage detection: (a) the distribution of prediction error; (b) the *UCL* thresholds.

RMSE values to secure the high accuracy of damage detection. Comparing with the loss values of the proposed model shown in Fig. 9(a), the loss values of Ai's model are significantly higher. Figure 15(c) illustrates the testing *RMSE* across 5 folds, ranging from 0.1042 to 0.1049, with a mean of 0.1045, equivalent to approximately 10% of the *DI* of damaged locations. The testing *MSE* across 5 folds, with a mean of 0.0109, is depicted in Fig. 15(d), while the testing *MAE* across 5 folds, with a mean of 0.0457, is illustrated in Fig. 15(e).

Several typical damage identification results are depicted in Fig. 16. Compared to the diagnostic results of the proposed method presented in Fig. 12, the accuracy of Ai's model is lower. While the proposed model predicts the *DI* values near 1 for damaged locations, Ai's model predicts values in the range of 0.2–0.6 (Figs. 16(a)–16(c). Additionally, although the damaged locations yield relatively higher *DI* values than undamaged locations, other locations also show equivalent *DI* values.

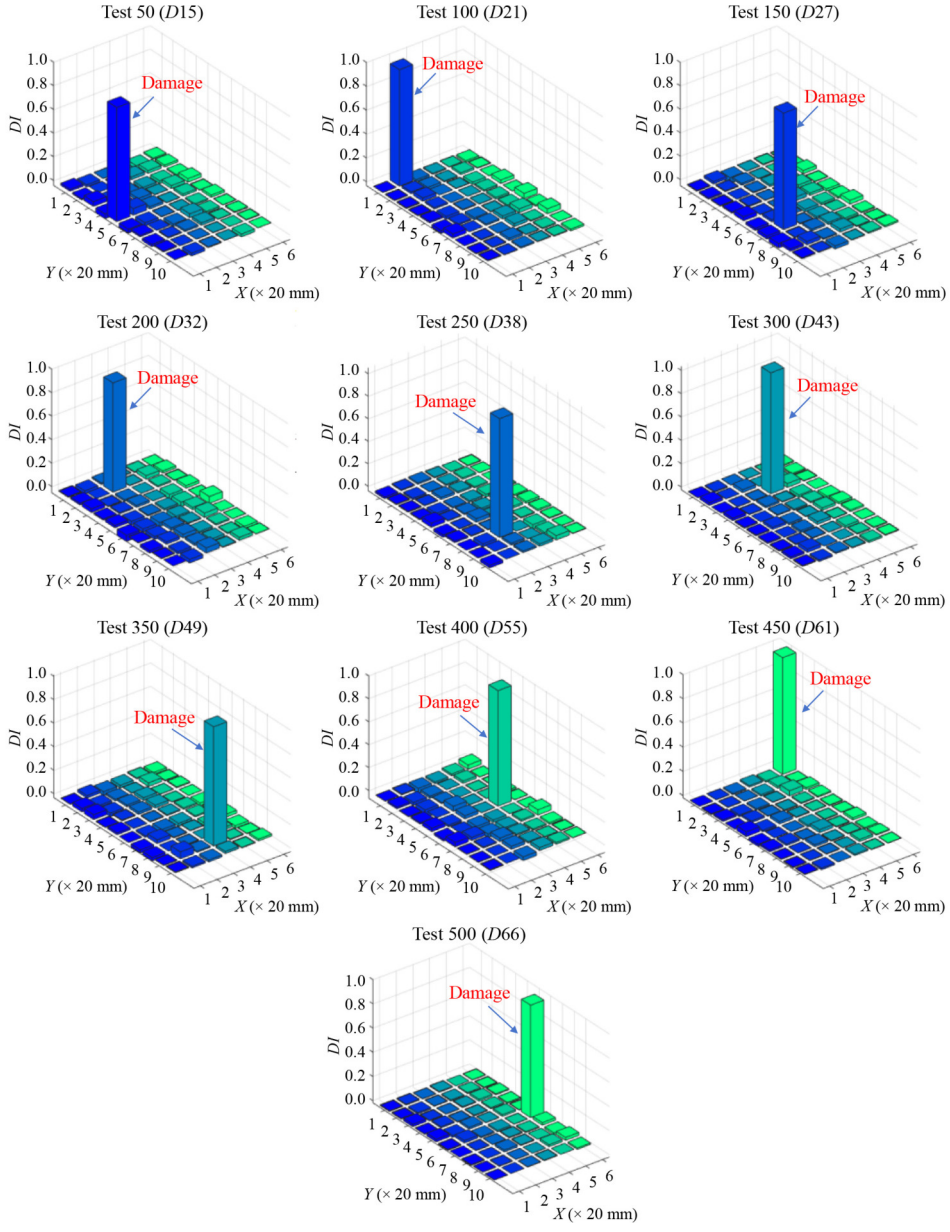

Fig. 12 Some typical prediction results by the proposed method.

5.3.2 Nguyen's model

The architecture of the 1D CNN model introduced by Nguyen et al. [38] was adjusted to accommodate the EMA data set. Figure 17 displays the training loss and evaluation outcomes across 5 folds for Nguyen's method. In all folds, a considerable reduction in loss is evident during the initial 500 training iterations (Fig. 17(a)). Subsequently, the loss gradually decreases over the next 3500 iterations (Fig. 17(b)), with the final iterations showing a variation primarily between 0.4 and 0.5. In comparison to the loss values of the proposed model shown in Fig. 9(a), the losses of Nguyen's model are notably higher. Figure 17(c) illustrates the testing *RMSE* across 5 folds, ranging from 0.1199 to 0.1237, with a mean of 0.1217, equivalent to approximately 12% of the *DI* of damaged locations. The testing *MSE* of 5 folds with a mean of 0.0148 and the testing *MAE* of 5 folds with a mean of 0.0377 are shown in Figs. 17(d) and 17(e), respectively.

Figure 18 presents typical damage identification results. In contrast to the diagnostic outcomes of the proposed method shown in Fig. 12, the accuracy of Nguyen's model is inferior. While the proposed model predicts *DI* values near 1 for damaged locations, Nguyen's model predicts *DI* values in the range of 0.15–0.6 only (Figs. 18(a)–18(c)). Moreover, undamaged locations exhibit *DI* values equivalent to those of damaged locations, posing challenges in pinpointing the location of damage in the plate.

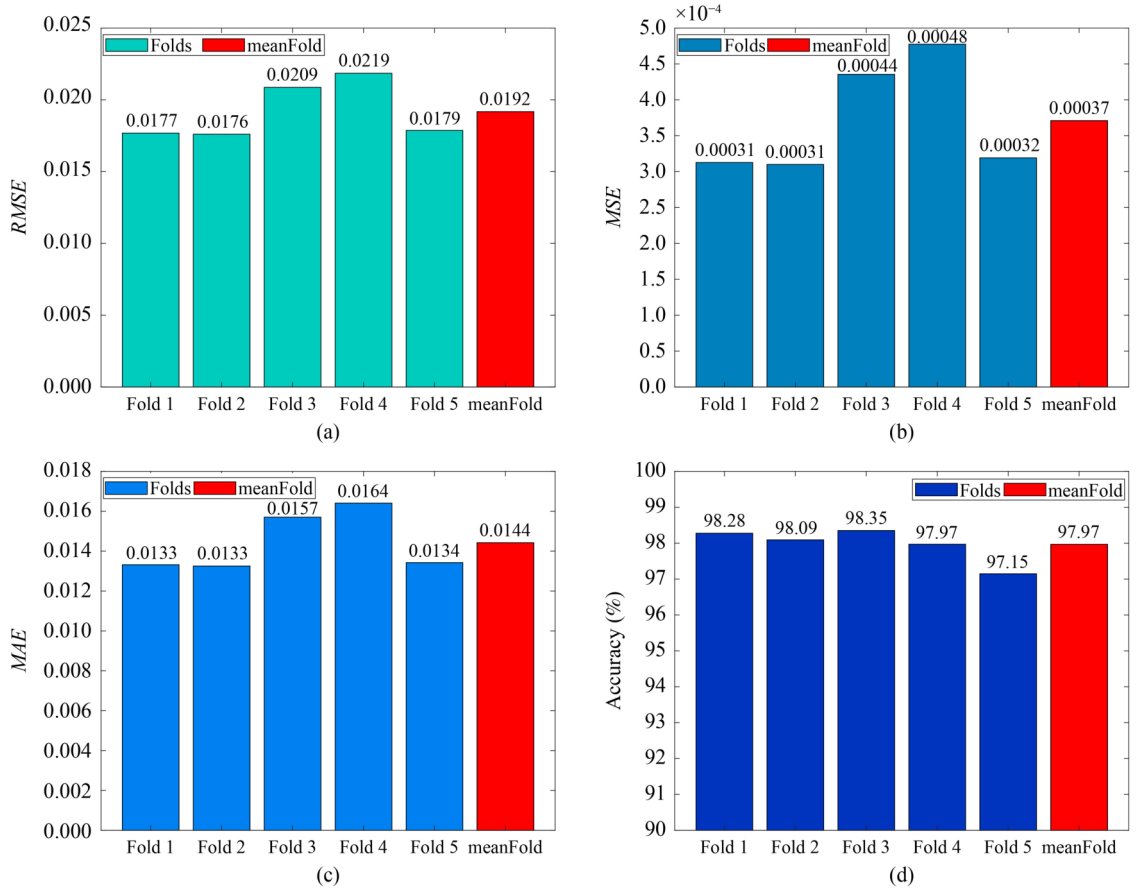

Fig. 13 Performance evaluation of the model: (a) the testing *RMSE* of 5 folds; (b) the testing *MSE* of 5 folds; (c) the testing *MAE* of 5 folds; (d) the testing accuracies of 5 folds.

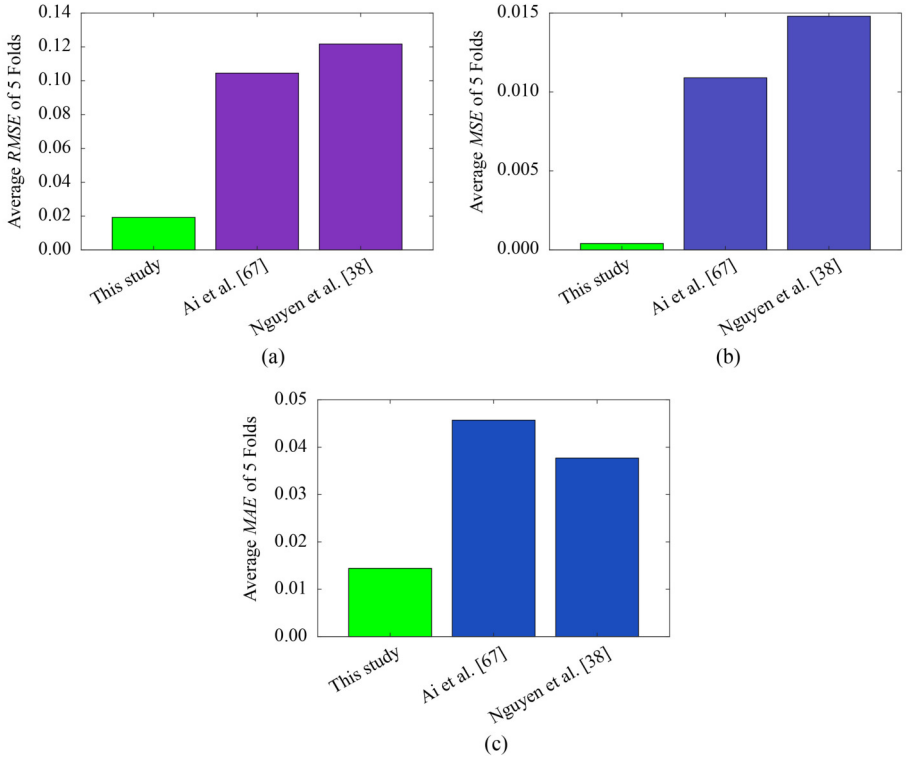

Fig. 14 Performance comparison between the proposed method and other 1D CNN models: (a) *RMSE*; (b) *MSE*; (c) *MAE*.

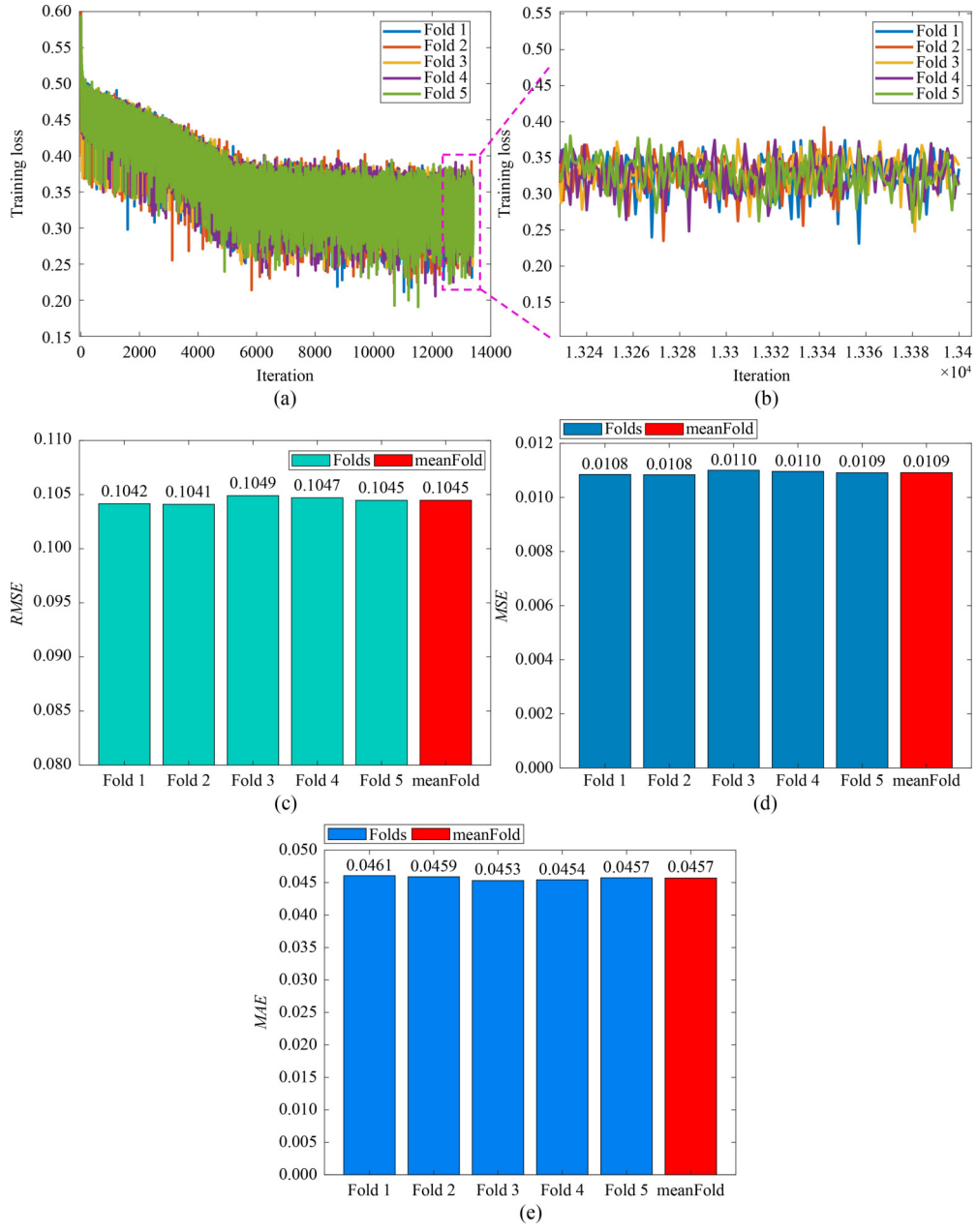

Fig. 15 The training loss and evaluation results across 5 folds of Ai's method: (a) the training loss; (b) the magnified loss; (c) the testing *RMSE*; (d) the testing *MSE*; (e) the testing *MAE*.

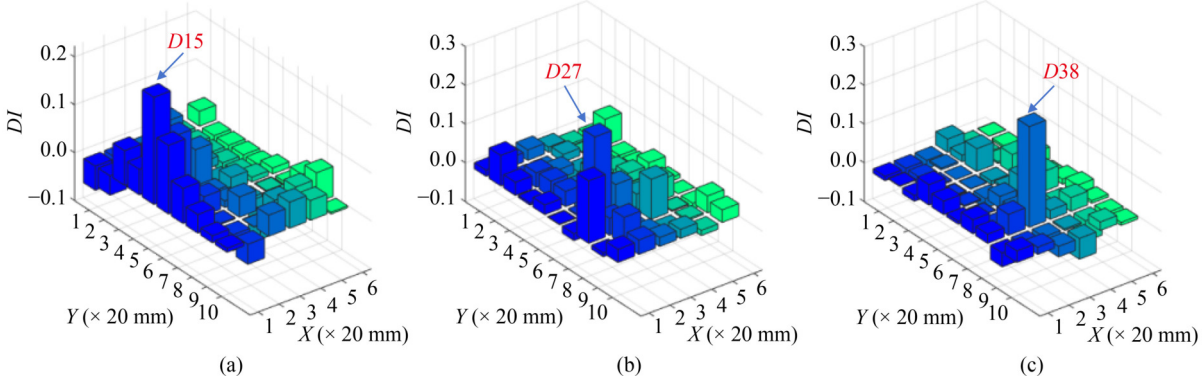

Fig. 16 Some typical damage prediction results by Ai's method: (a) Test 50 (D_{15}); (b) Test 150 (D_{27}); (c) Test 250 (D_{38}).

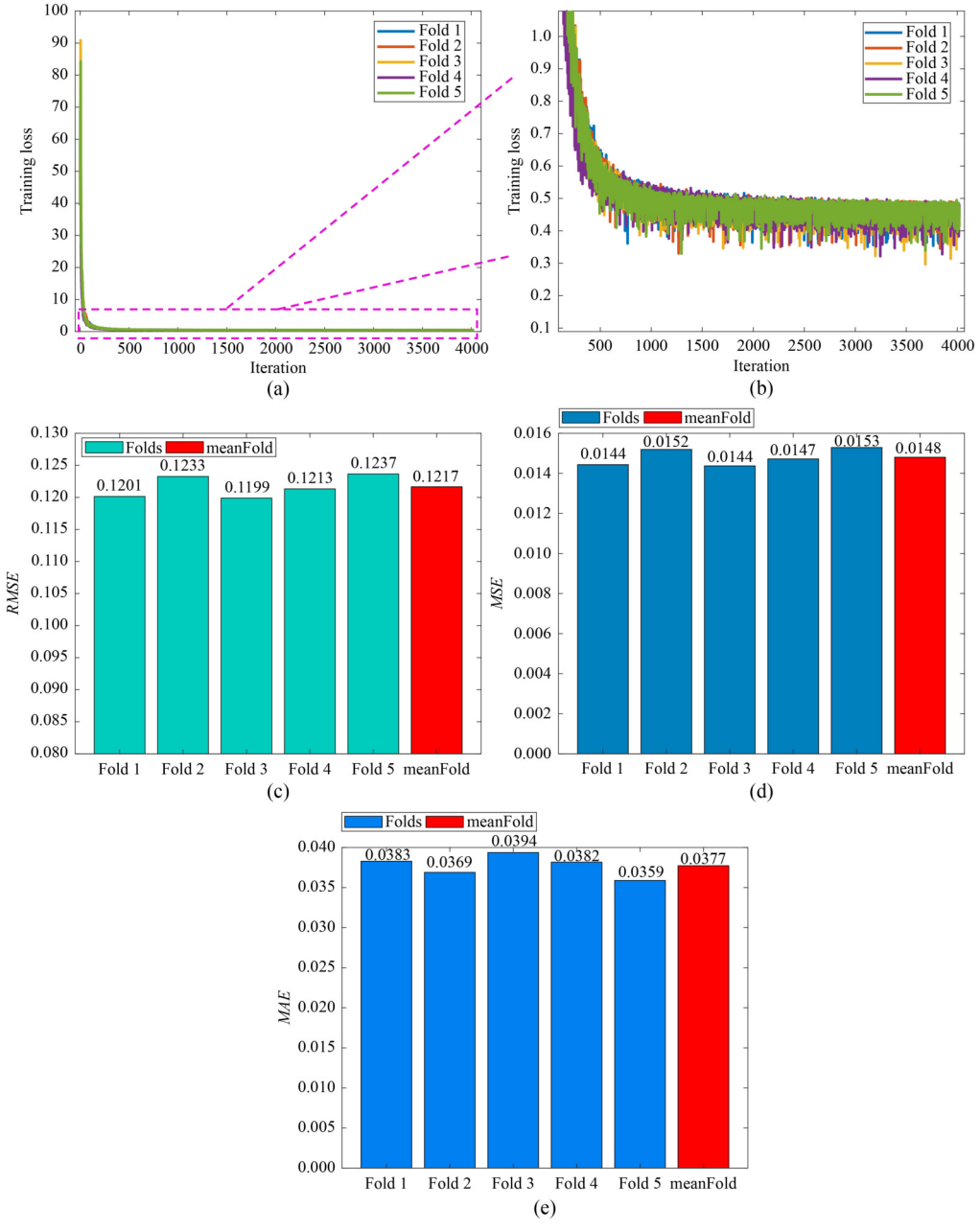

Fig. 17 The training loss and evaluation results across 5 folds of the Nguyen's method: (a) the training loss; (b) magnified loss; (c) the testing *RMSE*; (d) the testing *MSE*; (e) the testing *MAE*.

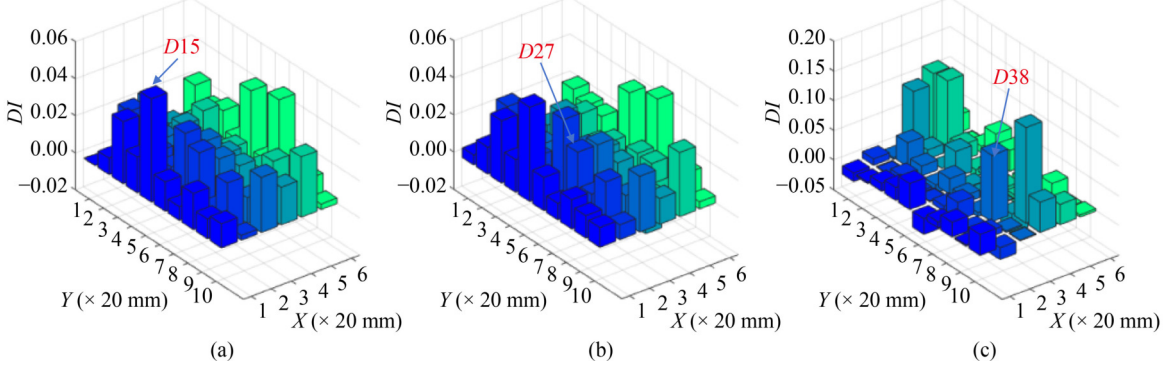

Fig. 18 Some typical damage prediction results by Nguyen's method: (a) Test 50 (D_{15}); (b) Test 150 (D_{27}); (c) Test 250 (D_{38}).

6 Conclusions

Conventional damage metrics employed in the admittance technique solely quantify changes in the EMA response through statistical measures, offering restricted insights into the damage location, especially in cases where damage introduces nonlinearities in EMA features. This study presents a new approach centered on the deep learning of raw EMA signals for robust damage localization in plate structures. Through the development of a 1D CNN-based regression model, the method automates the processing of raw EMA responses and predicts damage probabilities across multiple locations in a target plate. The validation process, conducted on a joint splice plate, involved measuring raw EMA responses at various damaged locations, augmenting the data set with white noise to simulate realistic measurement conditions, and utilizing K-fold cross-validation for training and testing the developed 1D CNN model. From the experimental study, the following concluding remarks can be drawn, as follows.

1) The proposed method achieves a high accuracy rate of 98% in identifying the state and location of damage in the joint splice plate.

2) Comparative analysis against the two established 1D CNN models demonstrates the superior performance of the proposed method, exhibiting significantly lower testing *RMSE*.

3) The method demonstrates a capability to directly handle raw EMA responses, overcoming limitations associated with traditional EMA-based approaches related to the selection of optimal high-frequency ranges and appropriate damage metrics.

4) By eliminating signal preprocessing steps, the proposed method holds substantial promise for real-time damage monitoring in plate structures.

5) The proposed method demonstrates the potential to monitor multiple damage locations in a plate structure using only a single transducer with a single measurement channel. This makes it a promising solution for cost-effective SHM through reducing data acquisition costs and enabling the implementation of low-cost EMA analyzers with a limited number of sensing channels.

Our forthcoming research endeavors will concentrate on extending the applicability of the proposed method. It is imperative to assess the method's performance in more intricate damage scenarios, including instances with multiple damage locations exhibiting varying extents of damage. Further investigations will be conducted to assess the effectiveness of the proposed method in the context of an *in situ* plate-like structures and to explore more realistic damage simulations, such as fatigue cracks and environmental corrosion. The comparison and the employment of different data augmentation methods will also be investigated in a future study.

Acknowledgements We acknowledge Ho Chi Minh City University of Technology (HCMUT), VNU-HCM for supporting this study.

Competing interests The authors declare that they have no competing interest.

References

1. Park G, Inman D J. Impedance-based structural health monitoring. In: Proceedings of SPIE. Bellingham: SPIE, 2017
2. Chaudhry Z, Joseph T, Sun F, Rogers C. Local-area health monitoring of aircraft via piezoelectric actuator/sensor patches. In: Proceedings of SPIE. Bellingham: SPIE, 1995
3. Park G, Cudney H H, Inman D J. Feasibility of using impedance-based damage assessment for pipeline structures. Earthquake Engineering & Structural Dynamics, 2001, 30(10): 1463–1474
4. Yang Y W, Lim Y Y, Soh C K. Practical issues related to the application of the electromechanical impedance technique in the structural health monitoring of civil structures: II. Numerical verification. Smart Materials and Structures, 2008, 17(3): 035009
5. Le T C, Luu T H T, Nguyen H P, Nguyen T H, Ho D D, Huynh T C. Piezoelectric impedance-based structural health monitoring of wind turbine structures: Current status and future perspectives. Energies, 2022, 15(15): 5459
6. Nguyen T C, Huynh T C, Yi J H, Kim J T. Hybrid bolt-loosening detection in wind turbine tower structures by vibration and impedance responses. Wind and Structures, 2017, 24(4): 385–403
7. Yang Y, Liu H, Annamdas V G M, Soh C K. Monitoring damage propagation using PZT impedance transducers. Smart Materials and Structures, 2009, 18(4): 045003
8. Nguyen T T, Hoang N D, Nguyen T H, Huynh T C. Analytical impedance model for piezoelectric-based smart Strand and its feasibility for prestress force prediction. Structural Control & Health Monitoring, 2022, 29(11): e3061
9. Park G, Farrar C R, Rutherford A C, Robertson A N. Piezoelectric active sensor self-diagnostics using electrical admittance measurements. Journal of Vibration and Acoustics, 2006, 128(4): 469–476
10. Park G, Sohn H, Farrar C R, Inman D J. Overview of piezoelectric impedance-based health monitoring and path forward. The Shock and Vibration Digest, 2003, 35(6): 451–463
11. Liu P, Lim H J, Yang S, Sohn H, Lee C H, Yi Y, Kim D, Jung J, Bae I. Development of a "stick-and-detect" wireless sensor node for fatigue crack detection. Structural Health Monitoring, 2016, 16(2): 153–163
12. Zhu H, Luo H, Ai D, Wang C. Mechanical impedance-based technique for steel structural corrosion damage detection. Measurement, 2016, 88: 353–359
13. Nguyen T T, Ta Q B, Ho D D, Kim J T, Huynh T C. A method for automated bolt-loosening monitoring and assessment using impedance technique and deep learning. Developments in the Built Environment, 2023, 14: 100122
14. Madi E, Pope K, Huang W, Iqbal T. A review of integrating ice detection and mitigation for wind turbine blades. Renewable & Sustainable Energy Reviews, 2019, 103: 269–281

15. Perera R, Pérez A, García-Diéguez M, Zapico-Valle J. Active wireless system for structural health monitoring applications. Sensors, 2017, 17(12): 2880
16. Pham Q Q, Ta Q B, Park J H, Kim J T. Raspberry Pi platform wireless sensor node for low-frequency impedance responses of PZT interface. Sensors, 2022, 22(24): 9592
17. Min J, Park S, Yun C B, Song B. Development of a low-cost multifunctional wireless impedance sensor node. Smart Structures and Systems, 2010, 6(5–6): 689–709
18. Zagrai A N, Giurgiutiu V. Electro-mechanical impedance method for crack detection in thin plates. Journal of Intelligent Material Systems and Structures, 2001, 12(10): 709–718
19. Giurgiutiu V, Zagrai A, Jing Bao J. Piezoelectric wafer embedded active sensors for aging aircraft structural health monitoring. Structural Health Monitoring, 2002, 1(1): 41–61
20. Park G, Inman D J. Structural health monitoring using piezoelectric impedance measurements. Philosophical Transactions—Royal Society. Mathematical, Physical, and Engineering Sciences, 2007, 365(1851): 373–392
21. Tinoco H A, Robledo-Callejas L, Marulanda D J, Serpa A L. Damage detection in plates using the electromechanical impedance technique based on decoupled measurements of piezoelectric transducers. Journal of Sound and Vibration, 2016, 384: 146–162
22. Tawie R, Park H B, Baek J, Na W S. Damage detection performance of the electromechanical impedance (EMI) technique with various attachment methods on glass fibre composite plates. Sensors, 2019, 19(5): 1000
23. Le B T, Nguyen T T, Truong T D N, Nguyen C T, Phan T T V, Ho D D, Huynh T C. Crack detection in bearing plate of prestressed anchorage using electromechanical impedance technique: A numerical investigation. Buildings, 2023, 13(4): 1008
24. Zhu J, Qing X, Liu X, Wang Y. Electromechanical impedance-based damage localization with novel signatures extraction methodology and modified probability-weighted algorithm. Mechanical Systems and Signal Processing, 2021, 146: 107001
25. Min J, Park S, Yun C B. Impedance-based structural health monitoring using neural networks for autonomous frequency range selection. Smart Materials and Structures, 2010, 19(12): 125011
26. Huynh T C, Kim J T. Compensation of temperature effect on impedance responses of PZT interface for prestress-loss monitoring in PSC girders. Smart Structures and Systems, 2016, 17(6): 881–901
27. Huynh T C, Dang N L, Kim J T. Advances and challenges in impedance-based structural health monitoring. Structural Monitoring and Maintenance, 2017, 4(4): 301–329
28. Lopes V Jr, Park G, Cudney H H, Inman D J. Impedance-based structural health monitoring with artificial neural networks. Journal of Intelligent Material Systems and Structures, 2000, 11(3): 206–214
29. Huynh T C, Kim J T. RBFN-based temperature compensation method for impedance monitoring in prestressed tendon anchorage. Structural Control and Health Monitoring, 2018, 25(6): e2173
30. Guo, H. , X. Zhuang, and T. Rabczuk, A deep collocation method for the bending analysis of Kirchhoff plate. Computers Materials & Continua, 2019, 59(2): 433–456
31. Samaniego E, Anitescu C, Goswami S, Nguyen-Thanh V M, Guo H, Hamdia K, Zhuang X, Rabczuk T. An energy approach to the solution of partial differential equations in computational mechanics via machine learning: Concepts, implementation and applications. Computer Methods in Applied Mechanics and Engineering, 2020, 362: 112790
32. Zhuang X, Guo H, Alajlan N, Zhu H, Rabczuk T. Deep autoencoder based energy method for the bending, vibration, and buckling analysis of Kirchhoff plates with transfer learning. European Journal of Mechanics A—Solids, 2021, 87: 104225
33. Hamdia K M, Ghasemi H, Bazi Y, AlHichri H, Alajlan N, Rabczuk T. A novel deep learning based method for the computational material design of flexoelectric nanostructures with topology optimization. Finite Elements in Analysis and Design, 2019, 165: 21–30
34. Guo H, Zhuang X, Chen P, Alajlan N, Rabczuk T. Stochastic deep collocation method based on neural architecture search and transfer learning for heterogeneous porous media. Engineering with Computers, 2022, 38(6): 5173–5198
35. Abdeljaber O, Avci O, Kiranyaz M S, Boashash B, Sodano H, Inman D J. 1-D CNNs for structural damage detection: Verification on a structural health monitoring benchmark data. Neurocomputing, 2018, 275: 1308–1317
36. Cha Y J, Choi W, Büyüköztürk O. Deep learning-based crack damage detection using convolutional neural networks. Computer-Aided Civil and Infrastructure Engineering, 2017, 32(5): 361–378
37. Huynh T C. Vision-based autonomous bolt-looseness detection method for splice connections: Design, lab-scale evaluation, and field application. Automation in Construction, 2021, 124: 103591
38. Nguyen T T, Tuong Vy Phan T, Ho D D, Man Singh Pradhan A, Huynh T C. Deep learning-based autonomous damage-sensitive feature extraction for impedance-based prestress monitoring. Engineering Structures, 2022, 259: 114172
39. Li G, Luo M, Huang J, Li W. Early-age concrete strength monitoring using smart aggregate based on electromechanical impedance and machine learning. Mechanical Systems and Signal Processing, 2023, 186: 109865
40. Ai D, Mo F, Han Y, Wen J. Automated identification of compressive stress and damage in concrete specimen using convolutional neural network learned electromechanical admittance. Engineering Structures, 2022, 259: 11476
41. Ai D, Cheng J. A deep learning approach for electromechanical impedance based concrete structural damage quantification using two-dimensional convolutional neural network. Mechanical Systems and Signal Processing, 2023, 183: 109634
42. Zhang X, Wang H, Hou B, Xu J, Yan R. 1D-CNN-based damage identification method based on piezoelectric impedance using adjustable inductive shunt circuitry for data enrichment. Structural Health Monitoring, 2022, 21(5): 1992–2009
43. Ta Q B, Pham Q Q, Pham N L, Huynh T C, Kim J T. Smart aggregate-based concrete stress monitoring via 1D CNN deep learning of raw impedance signals. Structural Control and Health Monitoring, 2024, 2024: 5822653.
44. de Oliveira M, Monteiro A, Vieira Filho J. A new structural health monitoring strategy based on PZT sensors and convolutional neural network. Sensors, 2018, 18(9): 2955
45. Bhalla S, Kiong Soh C. Structural impedance based damage

diagnosis by piezo-transducers. Earthquake Engineering & Structural Dynamics, 2003, 32(12): 1897–1916
46. Liang C, Sun F P, Rogers C A. Coupled electro-mechanical analysis of adaptive material systems-determination of the actuator power consumption and system energy transfer. Journal of Intelligent Material Systems and Structures, 1994, 5(1): 12–20
47. Park S, Yi J H, Yun C B, Roh Y R. Impedance-based damage detection for civil infrastructures. KSCE Journal of Civil Engineering, 2004, 8(4): 425–433
48. Kim J T, Park J H, Hong D S, Park W S. Hybrid health monitoring of prestressed concrete girder bridges by sequential vibration-impedance approaches. Engineering Structures, 2010, 32(1): 115–128
49. Min J, Park S, Yun C B, Lee C G, Lee C. Impedance-based structural health monitoring incorporating neural network technique for identification of damage type and severity. Engineering Structures, 2012, 39: 210–220
50. Kang D, Benipal S S, Gopal D L, Cha Y J. Hybrid pixel-level concrete crack segmentation and quantification across complex backgrounds using deep learning. Automation in Construction, 2020, 118: 103291
51. Acharya U R, Fujita H, Oh S L, Hagiwara Y, Tan J H, Adam M. Application of deep convolutional neural network for automated detection of myocardial infarction using ECG signals. Information Sciences, 2017, 415: 190–198
52. Singh D, Singh B. Investigating the impact of data normalization on classification performance. Applied Soft Computing, 2020, 97(B): 105524
53. Mattioli F, Porcaro C, Baldassarre G. A 1D CNN for high accuracy classification and transfer learning in motor imagery EEG-based brain-computer interface. Journal of Neural Engineering, 2021, 18(6): 066053
54. Agarap A F. Deep learning using rectified linear units (ReLu). 2018, arXiv:1803.08375
55. Gholamalinezhad H, Khosravi H. Pooling methods in deep neural networks: A review. 2020, arXiv:2009.07485
56. Huynh T C, Kim J T. Quantification of temperature effect on impedance monitoring via PZT interface for prestressed tendon anchorage. Smart Materials and Structures, 2017, 26(12): 125004
57. Ma S L, Jiang S F, Li J. Structural damage detection considering sensor performance degradation and measurement noise effect. Measurement, 2019, 131: 431–442
58. Huynh T C, Nguyen T D, Ho D D, Dang N L, Kim J T. Sensor fault diagnosis for impedance monitoring using a piezoelectric-based smart interface technique. Sensors, 2020, 20(2): 510
59. Helstrom C W. The resolution of signals in white, Gaussian noise. In: Proceedings of the IRE, New York: IEEE, 1955, 1111–1118
60. Campeiro L M, da Silveira R Z M, Baptista F G. Impedance-based damage detection under noise and vibration effects. Structural Health Monitoring, 2017, 17(3): 654–667
61. de Castro B, Baptista F, Ciampa F. New imaging algorithm for material damage localisation based on impedance measurements under noise influence. Measurement, 2020, 163: 107953
62. Jung Y. Multiple predicting K-fold cross-validation for model selection. Journal of Nonparametric Statistics, 2018, 30(1): 197–215
63. Nguyen K D, Kim J T. Smart PZT-interface for wireless impedance-based prestress-loss monitoring in tendon-anchorage connection. Smart Structures and Systems, 2012, 9(6): 489–504
64. Huynh T C, Lee K S, Kim J T. Local dynamic characteristics of PZT impedance interface on tendon anchorage under prestress force variation. Smart Structures and Systems, 2015, 15(2): 375–393
65. Behmanesh I, Moaveni B. Probabilistic identification of simulated damage on the Dowling Hall footbridge through Bayesian finite element model updating. Structural Control and Health Monitoring, 2015, 22(3): 463–483
66. Rajendran P, Srinivasan S M. Identification of added mass in the composite plate structure based on wavelet packet transform. Strain, 2016, 52(1): 14–25
67. Ai D, Mo F, Cheng J, Du L. Deep learning of electromechanical impedance for concrete structural damage identification using 1-D convolutional neural networks. Construction & Building Materials, 2023, 385: 131423